GNSS-RO Residual Ionospheric Error (RIE): A New Method and Assessment

Dong L. Wu[1], Valery A. Yudin[2], Kyu-Myong Kim[1], Mohar Chattopadhyay[3], Lawrence Coy[3], Ruth S. Lieberman[1], C. C. Jude H. Salinas[4], Jae N. Lee[5], Jie Gong[1], and Guiping Liu[1]

[1]NASA Goddard Space Flight Center, Greenbelt, MD 20771, USA
[2]Department of Physics, The Catholic University of America, Washington, DC 20064, USA
[3]Science Systems and Applications Inc., Lanham, MD 20706, USA
[4]GESTAR-II, University of Maryland Baltimore County, MD 21250, USA
[5]JCET, University of Maryland Baltimore County, MD 21250, USA

Correspondence to: Dong.L.Wu (dong.l.wu@nasa.gov)

Abstract.

GNSS radio occultation (RO) observations play an increasingly important role in monitoring climate changes and numerical weather forecasts in the upper troposphere and stratosphere. The magnitudes of the RO bending angle are small at these altitudes, and therefore residual ionospheric error (RIE) is critical to accurately retrieve atmospheric temperature and refractivity. The latter represent the state variables of the weather and climate models. RIEs remain poorly characterized in terms of the global geographical distribution and its variations with the local time and altitude influenced by the solar cycle and solar-geomagnetic disturbances. In this study we developed a new method to determine RIE from the RO excess phase measurement on a profile-by-profile basis. The method, called ϕ_{ex}-gradient ($d\phi_{ex}/dh_t$) method, is self-sufficient and based on the vertical derivative of the RO excess phase (ϕ_{ex}) with respect to tangent height (h_t), which can be applied to individual RO bending angle observations for RIE correction. In addition to the RIE in bending angle measurements, RIEs are found in the RO ϕ_{ex} measurements in the upper atmosphere where an exponential dependence is expected and in small-scale temperature variance of the RO retrieval. We found that the RIE values derived from the $d\phi_{ex}/dh_t$ method can be both positive and negative, which is fundamentally different from the κ-method that produces only the positive RIE values. The new algorithm reveals a latitude-dependent diurnal variation with a larger daytime negative RIE (up to ~3 μrad) in the tropics and subtropics. Based on the observed RIE climatology, a local-time dependent RIE representation is used to evaluate its impacts on reanalysis data.   We examined these impacts by comparing the data from the Goddard Earth Observing System (GEOS) data assimilation (DA) system with and without the RIE. The RIE impact on GEOS DA temperature is mainly confined to the polar regions of stratosphere. Between 10 hPa and 1 hPa the temperature differences are ~1K and exceed ~3-4 K in some cases. These results further highlight the need for RO RIE correction in the modern DA systems.

Keywords: residual ionospheric error, GNSS radio occultation, bending angle, data assimilation, reanalysis, climate data record, upper stratosphere, long-term variation

1   Introduction

The global navigation satellite system (GNSS) radio occultation (RO) data have been assimilated at numerical weather

65   prediction (NWP) centers for global and regional analysis/reanalysis using an observation operator such as the RO processing package (ROPP) [Culverwell et al. 2015]. Because of the high accuracy of RO measurements in the Upper Troposphere and Lower Stratosphere (UT/LS), GNSS-RO data become a valuable source of information in data assimilation (DA) systems for climate and weather predictions and applications [Foelsche et al., 2011; Kursinski et al., 1997]. Assimilating GNSS-RO vertical profiles of the bending angle (α or BA) was found to have significantly positive impacts on weather prediction skills

70   [Poli et al., 2010; Cucurull et al., 2013], both directly (through temperature and humidity in UT/LS) and indirectly (through radiance bias correction). Recent Observing System Simulation Experiments (OSSEs) suggest that the forecast skills would continue to improve with the increased global coverage and growth of GNSS-RO data without saturation [Harnisch et al., 2013; Prive et al., 2022].

However, the benefit of GNSS-RO data infusion requires ionospheric contributions to be fully removed for the α

75   measurements. The current algorithm to correct the ionospheric effects is to use a linear combination of the simultaneous RO measurements from two L-band frequencies (a.k.a, L1 and L2) [Vorob'ev and Krasil'nikova, 1994; Culverwell et al., 2015]. Although residual ionospheric errors (RIEs) after the correction are small in the α measurements, recent studies have found that they still have a significant impact on the DA with the RO observations. For example, Danzer et al. [2013] highlighted an unrealistic solar cycle variation in the mean neutral atmospheric temperature. Because the GNSS-RO data have been

80   increasingly assimilated in global analysis and reanalysis systems for climate records, it remains unclear to what extent RIEs may have affected the neutral atmospheric variables in terms of bias and unrealistic variability. The added variability in the DA products can be as important as their mean, because these DA data have been widely used to study atmospheric planetary and gravity waves.

Identifying the RIE sources, characterizing their amplitudes and developing a correction method have been an active field

85   of research. Higher-order ionospheric correction and propagation path differences are considered as the leading causes of the RIE. Without the dual-frequency first order (f^{-2}) correction, the ionospheric bending can induce in a pointing error of ~100 m in h_t and +/- 0.02° in BA [Hajj and Romans, 1998]. Ionospheric contributions are often not fully removed by the dual-frequency method, which depends on several factors. Most important factors include ionospheric structure [Ladreiter and Kirchengast 1996; Syndergaard 2000; Mannucci et al., 2011], magnetic field and electron density (Ne) [Hartmann and

90   Leitinger, 1984; Brunner and Gu, 1991; Morton et al., 2009; Hogan and Jakowski, 2011], radio wave propagation path

difference [Coleman and Forte, 2017], and horizontal inhomogeneity [Syndergaard and Kirchengast, 2022]. Among them, the ionospheric inhomogeneity and complex structural variability appear to be the key to many of the uncorrected RIEs. Depending on the underlying mechanism, the magnitudes of RIEs can vary from 10^{-8} rad to 10^{-6} rad in α. Because climate change signals are often small, it is imperative to characterize and reduce GNSS-RO RIEs as much as possible [Ringer and Healy, 2008; Gleisner et al., 2022].

Several methods have been proposed to correct RIEs in the α measurements before they are assimilated [Syndergaard 2000; Gorbunov, 2002; Healy and Culverwell, 2015; Zeng et al., 2016; Angling et al., 2018; Liu et al., 2020; Danzer et al., 2021]. Syndergaard [2000] emphasized the ionospheric E-layer impacts where the L1 and L2 may propagate through slightly different paths due to sharp vertical gradients at the lower ionosphere such as the sporadic-E. Such path differences can result in an error of as large as ~1 m in iono-free or atmospheric excess phase (ϕ_{ex}) measurements in the E-region or -0.3 μrad in α at h_t =60 km, but this error tends decrease gradually with h_t. Gorbunov [2002] developed an optimal estimation method, by balancing between the α measurement error and its climatology at high h_t, to reduce RIE impacts on the lower atmosphere. Healy and Culverwell [2015] introduced a so-called κ-method to remove high-order RIE contributions to α, which is proportional to the squared difference between L1 BA (α_1) and L2 BA α_2 or $\alpha_{RIE}(h_t) = \kappa \cdot (\alpha_1 - \alpha_2)^2$. The κ profile is estimated using realistic ionospheric *Ne* profiles, showing only negative RIEs values with a typical amplitude of 10-20 rad^{-1} [Healy and Culverwell, 2015; Angling et al., 2018]. From the open-loop (OL) tracking of L2C signal, Zeng et al. [2016] applied an empirical method for the ionospheric correction and extrapolate the $\alpha_1 - \alpha_2$ profile down to a very low h_t. Their extrapolation approach is similar to the κ-method, by fitting the $\alpha_1 - \alpha_2$ values at high-h_t. A slightly larger (between -10 and -30 μrad) were found for $\alpha_1 - \alpha_2$ at h_t =60 km. Angling et al. [2018] showed a similar amplitude (-10 μrad) for the $\alpha_1 - \alpha_2$ at h_t =60 km with a global ionosphere model. As a result, the κ method was extended globally as a function of solar zenith angle (χ) and solar cycle (F10.7). The κ model predicts a lower RIE value during the daytime and higher F10.7. Danzer et al. [2020] further implemented and evaluated the κ-model for RIE correction with the European Center for Medium-range Weather Forecast reanalysis (ERA-Interim, Dee et al., 2011; and ERA5, Hersbach et al., 2020), reporting warming ($0.2 - 2$ K) effects at 40-45 km. With a different modeling approach, however, Liu et al. [2020] showed much smaller values (< 0.1 μrad) of $\alpha_1 - \alpha_2$ at h_t =60 km. Using a 3D ray tracing technique, Li et al. [2020] found that the simulated RIE can be both positive and negative on the order of ±0.1 μrad. In summary, the current and recent studies display large differences in the estimated RIE amplitudes and morphologies. Thus, it remains unclear what spatiotemporal distribution is the correct representation of these RIEs and how these errors would impact on the assimilated data, in terms of local time and solar cycle variations, when the RIE-prone RO data are injected to DA systems.

In this study we developed a new method for RIE estimation, using the vertical gradient of RO ϕ_{ex} profile calculated at high h_t, hereinafter referred to as the ϕ_{ex}-gradient or $d\phi_{ex}/dh_t$ method. We show that $d\phi_{ex}/dh_t$ is directly related to the RIE-induced $\alpha_1 - \alpha_2$ difference, and the RIE value determined at high h_t can be extrapolated to the α measurements in the low h_t domain. Our analysis reveals a different morphology of the RIE from the estimated $\alpha_1 - \alpha_2$ in terms of diurnal cycle,

latitudinal variability and solar cycle dependence. Impacts of the diurnal and latitudinal variations of RIE specified by the $d\phi_{ex}/dh_t$ method is assessed by performing the DA experiments with and without the RO RIE in the Goddard Earth Observing System for Instrument Teams (GEOS-IT).

2   GNSS-RO Data

2.1   Bending Angle (α) and Excess Phase (ϕ_{ex})

Bending of the RO ray path occurs where there exists a vertical gradient in refractive index, which can be from the ionosphere and the neutral atmosphere, and the bending angle is given by

$$\alpha = -2a \int_a^\infty \frac{1}{n\sqrt{n^2 r^2 - a^2}} \left(\frac{dn}{dr} \right) dr \tag{1}$$

where a is impact parameter, r is radius from the Earth center, and n is the refractive index from the group velocity of radio wave propagation. As discussed in detail by Wu [2018], the radio wave group and phase velocities have opposite effects on the excess phase measurement. The bending, which is the radio wave energy propagation with the group velocity, would cause the phase delay. On the other hand, the phase speed of radio wave propagation in plasma can exceed the light speed, causing a phase advance.

In the bending situation, if $dn/dr < 0$, as in the neutral atmosphere, the propagation ray is bended down towards the Earth ($\alpha < 0$). In the ionosphere the bending can be both upwards and downwards. In the top of ionosphere, where $dn/dr > 0$, the propagation ray tends to be bended upwards, whereas in the bottom of ionosphere, where $dn/dr < 0$, the ray is bended downwards by the vertical gradient of Ne. The ionospheric bending between GNSS transmitter and LEO (low Earth orbit) receiver depends on transmitter's radio wave frequency (f) while the neutral atmospheric bending is independent of the frequency. The first-order ionospheric bending effect can be removed using a linear combination of GNSS-RO processing [Vorob'ev and Krasil'nikova, 1994] as follows

$$\alpha = f_1^2/(f_1^2 - f_2^2) \cdot \alpha_1 - f_2^2/(f_1^2 - f_2^2) \cdot \alpha_2 \tag{2}$$

where f_1 and f_2 are L1 and L2 frequencies, and $f_1^2/(f_1^2 - f_2^2) = 2.5457$ and $f_2^2/(f_1^2 - f_2^2) = 1.5457$. In the absence of ionospheric bending, $\alpha = \alpha_1 = \alpha_2$, which is denoted by α_c as the correct value. In the case where the ionospheric bending effect is not completely removed by Eq.(2), an RIE exists in the α measurement, mathematically

$$\alpha = \alpha_c + \alpha_{RIE} \tag{3}$$

The phase advance in the ionospheric plasma propagation is often confused with the bending effect as an misconception, because it has the same f-dependence as in Eq.2, except with the opposite sign. Under this misconception, the phase advance contribution would be interpreted as an upward bending. Without modeling both phase delay (from bending) and phase advance (from radio propagation in plasma) accurately, the residual error can lead to a term α_{RIE} in Eq.3. Although α_{RIE} is expressed in bending angle unit, it may come from phase advance errors such as high-order f-dependence. Nevertheless, a phase advance error can occur from the indirect impact of a propagation path change even though the path length remains

155   same. In reality, the propagation path and phase advance differences coexist as the dual-frequency radio waves transverse through an inhomogeneous ionosphere [Appendix A].

    In this study we keep the conventional definition of RIE in terms of bending angle error, namely, α_{RIE}, but relate it the error of excess phase measurements that fundamentally causes α_{RIE}. In a simplified wave propagation model, Melbourne (2004) obtained a first-order linear relation between α and the excess Doppler (i.e., ϕ_{ex} derivative with respect to time),

160
$$\alpha \cong -\frac{d\phi_{ex}}{dt} \cdot \frac{1}{V_\perp} \tag{4}$$

where $V_\perp$ is the LEO motion perpendicular to its line of sight (LOS) to the GNSS transmitter. The atmospheric ϕ_{ex} can be obtained from L1 ($\phi_{ex_{L1}}$) and L2 ($\phi_{ex_{L2}}$) phase measurements with the linear combination similar to Eq.(2)

$$\phi_{ex} = f_1^2/(f_1^2 - f_2^2) \cdot \phi_{ex_{L1}} - f_2^2/(f_1^2 - f_2^2) \cdot \phi_{ex_{L2}} \tag{5}$$

For a rising/setting occultation, $V_\perp$ is the ascending/descending rate of RO sampling with respect to h_t, or the GNSS–LEO

165   straight line height (SLH), which yields $V_\perp \cong dh_t/dt$. In the upper atmosphere $V_\perp$ is typically ~2 km/s. Substituting this $V_\perp$-h_t relation into Eq.(4), we have

$$\alpha \cong -d\phi_{ex}/dh_t \tag{6}$$

In the upper atmosphere where there is little bending (i.e., $\alpha_c \approx 0$), a significant non-zero component in $d\phi_{ex}/dh_t$ indicates the existence of α_{RIE}. Here, $d\phi_{ex}/dh_t$ can be both positive and negative but not necessarily from bending only. Thus, Eq.(6)

170   is used as a theoretical basis in this study to derive α_{RIE} from the GNSS-RO Level-1B $\phi_{ex_{L1}}$ and $\phi_{ex_{L2}}$ data.

2.2   RIE and Detection Method

    For accurate estimation of the climate temperature trends from the GNSS-RO, it is important to identify, characterize and correct the RIE in the observed α profiles. At high altitudes, where magnitudes of RIEs may equal or/and exceed the background α values, the observed α noise significantly vary from profile to profile. As shown in Figs.1-3, the oscillatory

175   nature of α profile between 60 and 80 km preclude it from utilizing the α profile to reliably determine the RIE. In the case in Fig.1, a positive bias might exist in the mean α value at 60-80 km, whereas it is not a clear case in Fig.2 where an E-layer may have contaminated the profile. In addition, the atmospheric bending remains non-negligible at 60 km. Thus, in this study we focus on the estimation of RIE using the RO data at heights above 65 km.

    Although ionosphere-induced α oscillations in α_1 and α_2 are largely removed by Eq.(2), RIEs can occur at various

180   obviously associated with the α_1 and α_2 oscillations, while the larger negative one near 70-74 km are all correlated. These residuals can be readily traced back to the ϕ_{ex} measurements and their height derivatives. Another example is a step jump of the ϕ_{ex} profile at ~70 km in Fig.3, which results in a large and sharp spike in α. Despite the high (100-Hz) sampling rate of COSMIC-2 GNSS-RO, which helps to remove more ionospheric effects than the data from a lower sampling, these RIE signatures can still be seen in the in α and ϕ_{ex} profiles. On one hand, the sharp α spikes like those in Figs.2-3 may not play a

185   significant role in the lower atmosphere, because these RIEs tend to be confined near the spike altitude. On the other hand, as seen in Fig.4, the spike from the sporadic-E (Es) superimposed on a systematic slope ($d\phi_{ex}/dh_t$) should be considered as an

RIE. This extended slope appears to originate from the ionosphere above ~100 km (Fig 4c) and can affect the α measurements far below 100 km.
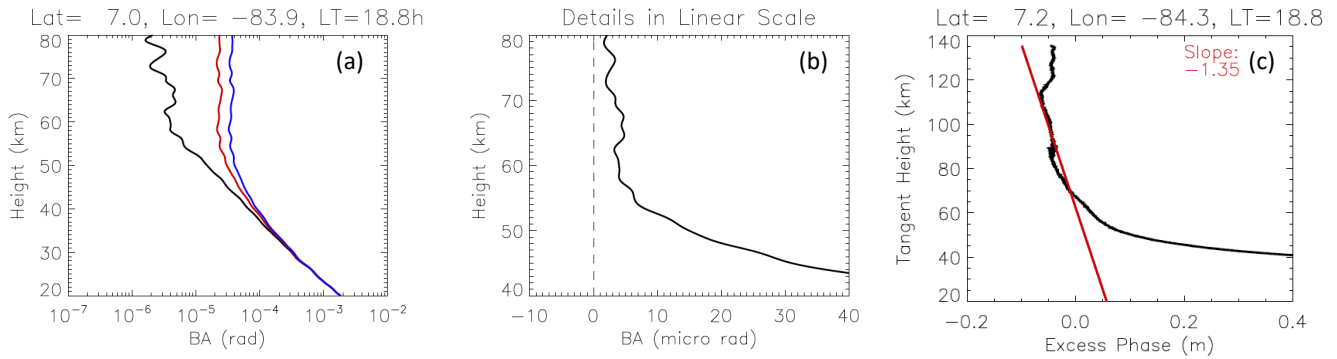
Fig.1. An example of COSMIC-2 atmospheric α profiles in (a) logarithmic and (b) linear scale, and (c) the corresponding ϕ_{ex} profile from January 1, 2022. The red and blue profiles in (a) are L1 and L2 α respectively. The dashed line in (b) denotes no RIE if the α average at 60-80 km is zero. The red line in (c) is a linear fit to the α data between 65 and 120 km, of which the slope is $d\phi_{ex}/dh_t$.
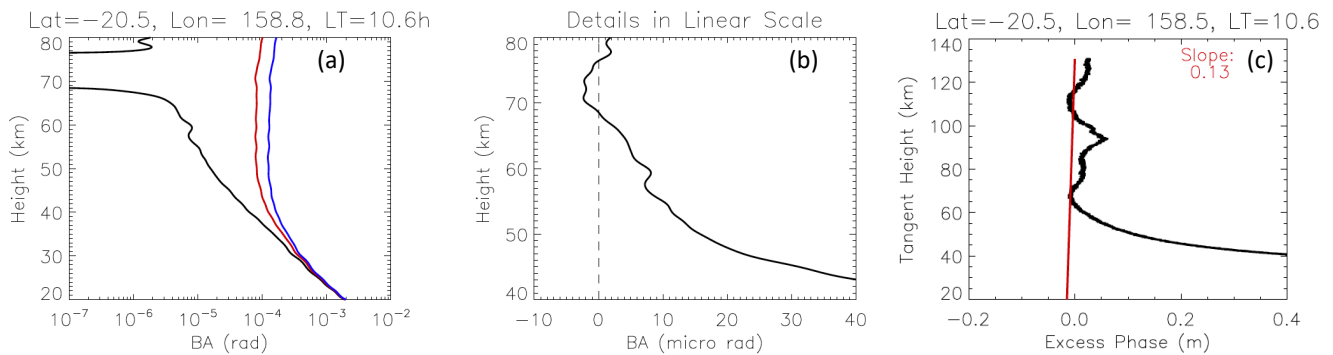
Fig.2. As in Fig.1 but for another example where an ionospheric E-layer is present in the ϕ_{ex} profile.
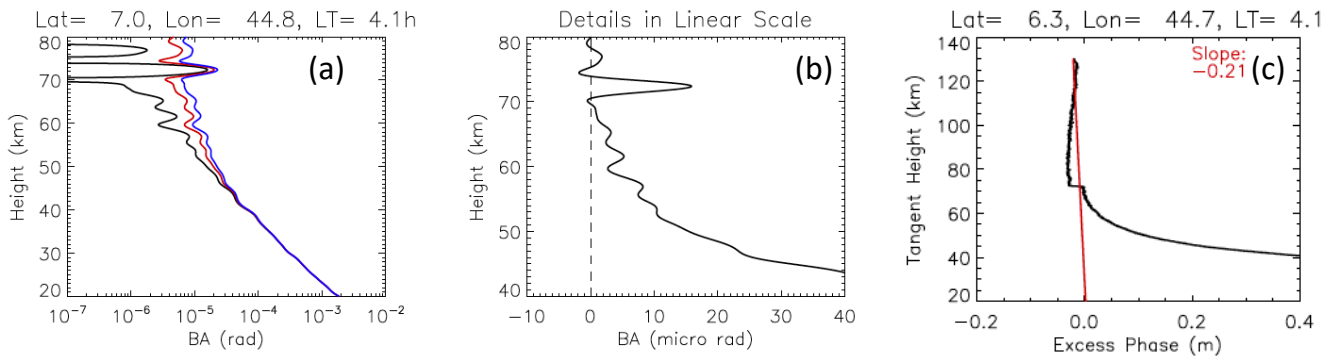
Fig.3. As in Fig.1 but for a case with a sharp jump in the ϕ_{ex} profile near 70 km and a moderate derivative $d\phi_{ex}/dh_t$.
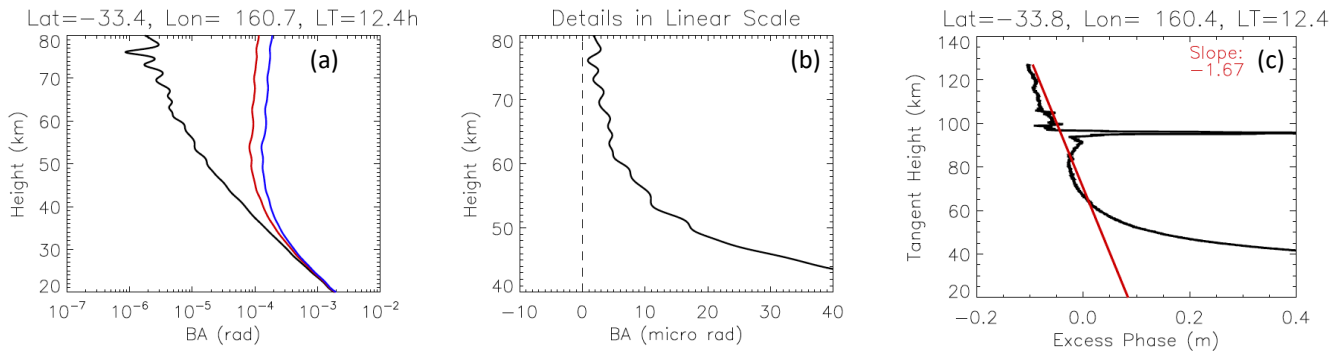
Fig.4. As in Fig.1 but for a case with a sharp spike in the ϕ_{ex} profile near 95 km and a significant derivative $d\phi_{ex}/dh_t$.

It is important to develop a method that can overcome the noisy/oscillatory nature of α profiles and estimate the RIE that may have an impact on the temperature retrieval in the upper troposphere and stratosphere. A robust RIE algorithm needs to demonstrate the following capabilities: (i) to adequately handle short/sharp spikes in the E-region; (ii) to be self-sufficient in determining the RIE for each individual α profile, regardless of the ionospheric conditions; and (iii) to be able to estimate the RIE in the presence of large noise. Using the relationship between the α and $d\phi_{ex}/dh_t$ as described by [Eq.6], we introduce a RIE correction scheme for the α profile, which can be implemented at Level-1B ϕ_{ex} (excess phase) processing. There are several advantages to use the Level-1B data for the RIE correction. They are as follows:

1. ϕ_{ex} is a more fundamental measurement than α. As discussed above, other processes in the radio wave propagation can induce RIEs even in the situation without bending. Thus, both positive and negative values are physically meaningful and allowed for $d\phi_{ex}/dh_t$.

2. The inversion from ϕ_{ex} to α profile in RO data reduction can introduce additional noise, which can make the RIE estimation more difficult. The ϕ_{ex} data do not contain the smoothing parameter and a priori constraints needed in the inversion algorithms. These parameters can affect the RIE determination since they may vary significantly between software developers and versions. In the $d\phi_{ex}/dh_t$ method, the least-squared linear fit to the iono-free ϕ_{ex} profile can use quality control applied directly to the Level-1B data.

3. ϕ_{ex} contains the information in the L1 ($\phi_{ex_{L1}}$) and L2 ($\phi_{ex_{L2}}$) measurements independently, rather than the corrected profile from Eq.5. The original Level-1B data with the high-rate sampling is retained useful insights and allow further investigations on the cause(s) of RIEs.

To estimate the RIE for α, we carry out a linear fit to the iono-free ϕ_{ex} data at $h_t > 65$ km for each RO profile independently, i.e.

$$\phi_{ex} = -\Delta\alpha \cdot h_t + \phi_0 \qquad\qquad h_t > 65 \text{ km} \qquad\qquad (7)$$

where ϕ_0 is the constant from the fitting and the slope $\Delta\alpha \equiv -d\phi_{ex}/dh_t$. If there is no RIE, $\Delta\alpha = 0$. Large $\Delta\alpha \neq 0$ values are interpreted as an RIE for the α profile. The 65 km altitude cutoff in the $\Delta\alpha$ calculation is to ensure that the fitting will not be influenced by the neutral atmospheric bending. To compare with the RIE estimated from the κ-method, we simply multiply $(\Delta\alpha_1 - \Delta\alpha_2)^2$ with κ, where $\Delta\alpha_1$ and $\Delta\alpha_2$ are derived respectively from $\phi_{ex_{L1}}$ and $\phi_{ex_{L2}}$. As shown and discussed in the following section, there are important differences between the RIE climatologies derived from the κ-method and the $d\phi_{ex}/dh_t$ method. Note that Eq.7 does not rely on any auxiliary data/model such as the international reference ionosphere (IRI), nor assumes the spherical symmetry of electron density (Ne) profile. As shown in Mannucci et al. [2011] and Coleman and Forte [2017], the spherical symmetry assumption can become problematic for the RIE evaluation in the presence of complex ionospheric structures and small-scale variability of the ionosphere.

Quality control (QC) on the ϕ_{ex} data is required to ensure the fitting yields a reasonable $\Delta\alpha$. Table 1 summaries the QC flags and procedures applied to GNSS-RO data in the RIE estimation. Because of complex impacts from ionospheric variability, the ϕ_{ex} data processing algorithm needs to deal with large ϕ_{ex} oscillations properly, especially those non-monotonic profiles with multiple extremes at altitudes > 65 km. These extraordinary ϕ_{ex} profiles include multiple layers with different ϕ_{ex} slopes in between, large jumps in the measurement, noisy profiles due to ionospheric scintillations, and disturbances from Es layers. With the QC#1 and QC#2 criteria in Table 1, we ensure that a ϕ_{ex} profile has enough samples and good signal-to-noise ratio (SNR) at 60-120 km to yield a useful fit from Eq.7. Since the GNSS-RO L1 ($\phi_{ex_{L1}}$) and L2 ($\phi_{ex_{L2}}$) measurements do not have absolute calibration, they are first initialized using the top value of each RO profile. Hence, the ϕ_{ex} values at 60-120 km should not be too far from zero [Figs.1-4]. However, profiles with very large ϕ_{ex} values or large standard deviation about its mean do exist. To deal with these cases, QC#3 and OC#4 are applied to the ϕ_{ex} data prior to the fitting. As noted above, Eq.7 can handle a constant offset in the ϕ_{ex} data after the data are screened by QC#3, but QC#4 helps to minimize the impacts from data spikes (e.g., Es) and E-layer residuals (e.g., Fig.2). Based on our algorithm experiments (see the discussion section), the ϕ_{ex} profile is required to have a top reaching a sufficient high altitude for a reliable RIE estimate, to overcome the Es effects that are largely confined at 80-100 km. Lastly, the ϕ_{ex} data may have a large gap in the profile, which could also yield a problematic fit from Eq.7 and should be excluded (QC#6). In this study we are not interested in very large $\Delta\alpha$ values that are greater than 2000 µrad (QC#7).

Table 1. QC in ϕ_{ex} Data Processing for $\Delta\alpha$

QC#	Description	Threshold
1	Ensure that number of ϕ_{ex} at 60-120 km is sufficient	N > 200
2	Check if mean RO signal at 60-120 km is too weak	L1 SNR > 100
3	Check if mean ϕ_{ex} ($\overline{\phi_{ex}}$) at 60-120 km is too large	$\left|\overline{\phi_{ex}}\right| < 30$ m
4*	Exclude large deviations from the mean ($\phi_{ex} - \overline{\phi_{ex}}$) at $h_t > 65$ km	$\left|\phi_{ex} - \overline{\phi_{ex}}\right| < 0.05$ m

5*	Check the top h_t of RO profile	$h_t > 80$ km, 120 km, 170 km
7	Avoid profiles with large h_t gaps at 60-120 km	$|dh_t| < 2$ km
8	Retain only realistic $\Delta\alpha$ values	$|\Delta\alpha| < 2$ µrad

Note: *Thresholds in the QC#4 and QC#5 require further tests to achieve optical results.

3.   RIEs from ϕ_{ex}-Gradient Method

3.1 $\Delta\alpha$ Morphology

Statistical properties of the $\Delta\alpha$ estimated from the slope $(d\phi_{ex}/dh_t)$ at high altitudes vary with local time, latitude, season, and solar activity, and they may also differ from each other depending on RO receiver type. To examine the probability distribution from different RO receivers, we first derive $\Delta\alpha$ without imposing QC#4 in Table 1 and aggregate the monthly $\Delta\alpha$ data in terms of a normalized probability density function (PDF) as a function of latitude separately for both day and night. Because of large sampling differences , the PDFs are normalized to its peak value in each latitude bin. Figs. 5-8 show the results from COSMIC-1 (Jan 2013), COSMIC-2 (Jan 2022), Spire (Jan 2022), MetOp-B (Jan 2023) and FY3-E (Jan 2023). For comparisons under a similar environment, we chose 2013 and 2022-2023 when it had high solar activities. January is a generally higher Ne month in the southern hemisphere (SH) due to more solar illumination. The top height of GNSS-RO profiles is required to reach 120 km (QC#5) for these comparisons. No every GNSS-RO sensor has this high altitude coverage in the regular operation (e.g., MetOp and FY3). However, since early 2022 MetOp-B/C have begun to acquire GNSS-RO profiles above 120 km routinely. MetOp-B/C satellites have a sun-synchronous orbit with the equator-crossing-time (ECT) of (8-10h and 20-22h). Thus, the comparison of MetOp-B/C with the COSMIC-1 observations is feasible but from different solar maximum years and with different local time coverages. Both COSMIC-1 and COSMIC-2 constellations, as well as Spire, have a coverage of all local times over a period of one month. The new GNSS receivers on FY3-E (March 2022-present) have been providing the RO sampling with a top above 120 km with a varying ECT (4-6h and 16-18h).

The COSMIC-2 $\Delta\alpha$ PDFs show a slightly noisy or wider distribution compared to COSMIC-1 [Figs.5-6]. But both data reveal a larger (more positive) $\Delta\alpha$ RIE in the SH than in the northern hemisphere (NH). This hemispheric difference is more pronounced during the day than at night. The daytime low-latitude PDFs appear to have a longer tail at negative $\Delta\alpha$ values, which is consistent with the statistics from Spire data [Fig.7]. The Spire $\Delta\alpha$ PDFs have a width falling between COSMIC-1 and COSMIC-2, but show the similar hemispheric difference. The ϕ_{ex} measurement noise may contribute partly to the $\Delta\alpha$ spread but the RIE is considered as a major cause of the non-zero $\Delta\alpha$ and its standard deviation.

The $\Delta\alpha$ derived from the meteorological satellites (i.e., MetOp-B and FY3-E) [Figs.8-9], which have a weaker SNR (signal-to-noise ratio) and a higher orbital altitude compared to the COSMIC-1/2 and Spire constellations, tends to have a noisier PDF. It is unclear whether the noisier behavior is related to sampling/orbital parameters or to the RO receiver design and their observing environment on spacecraft. Since MetOp and FY3 employed very different receiver designs but have a

similar SNR to Spire, their $\Delta\alpha$ PDF difference from COSMIC and Spire might be related to the orbital altitude. Another factor is the receiver environment on the spacecraft. The RO receivers on COSMIC and Spire satellites are considered as the primary payload and do not have much interference from other instruments on board. Interference and multipath issues can be a susceptibility problem when the multiple instruments are onboard spacecraft like MetOp and FY3. Interferences from other radio frequencies and structures may affect the RO receiver performance for high-quality ionospheric measurements.
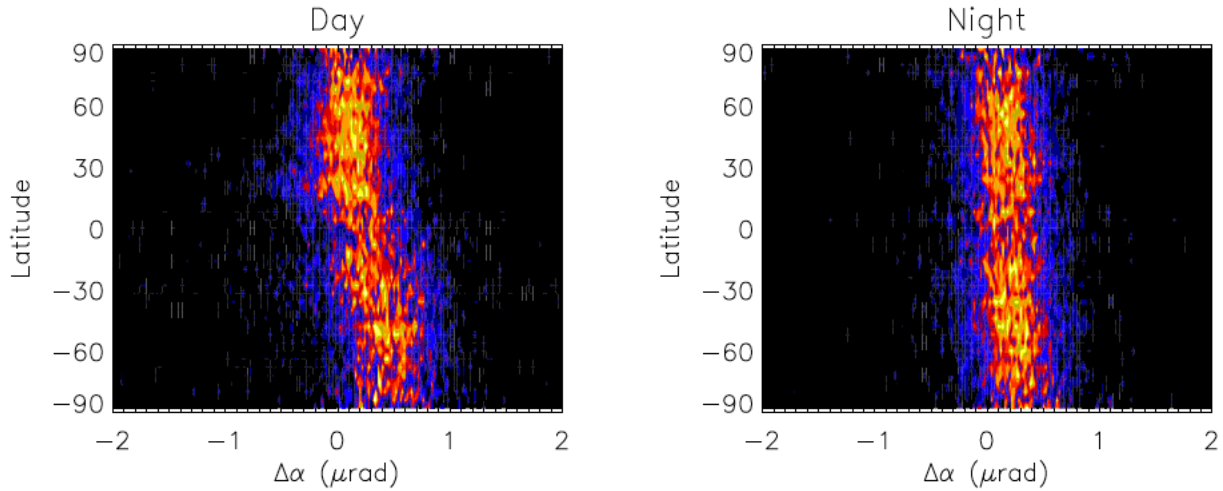
Fig.5 Latitude dependence of the probability density function (PDF) of COMSIC-1 $\Delta\alpha$ in μrad for day and night from Jan 2013. The PDF is normalized independently to its peak value at each 4° latitude bin. The PDF colors vary linearly between 0 (black) and 1 (yellow).
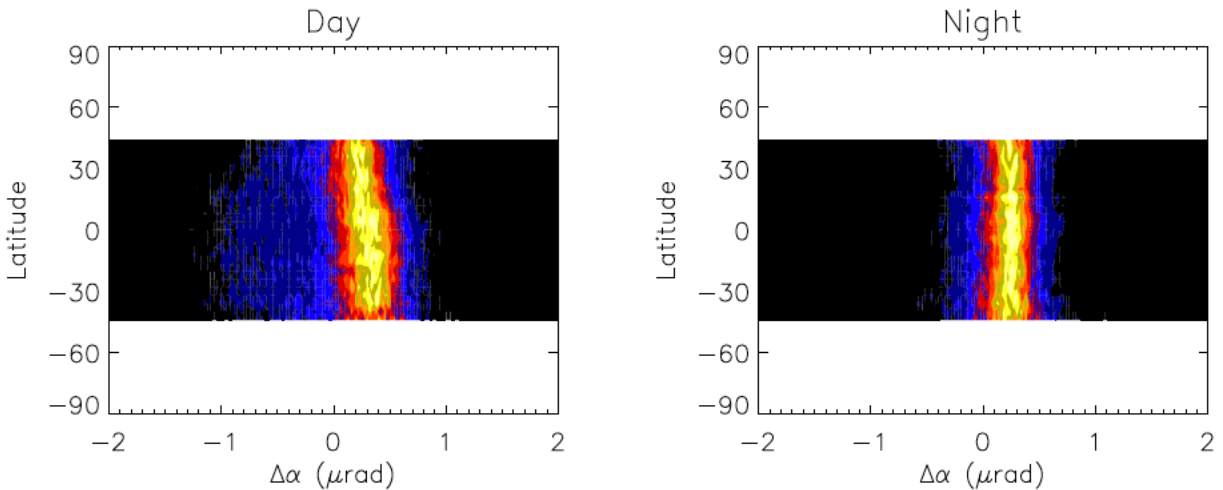
Fig.6. As in Fig.5 for COMSIC-2 from Jan 2022.
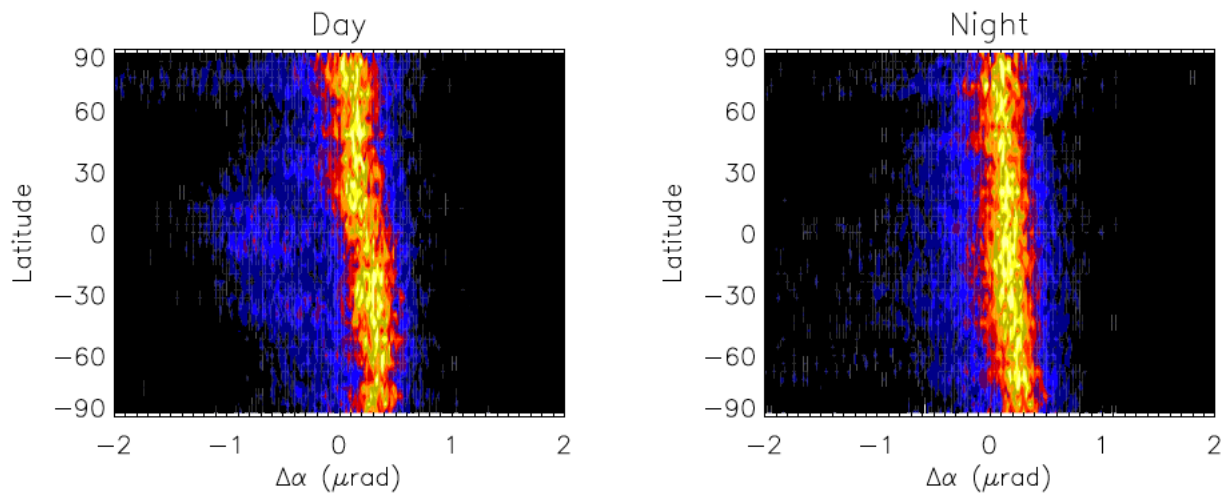
Fig.7. As in Fig.5 for Spire from Jan 2022.
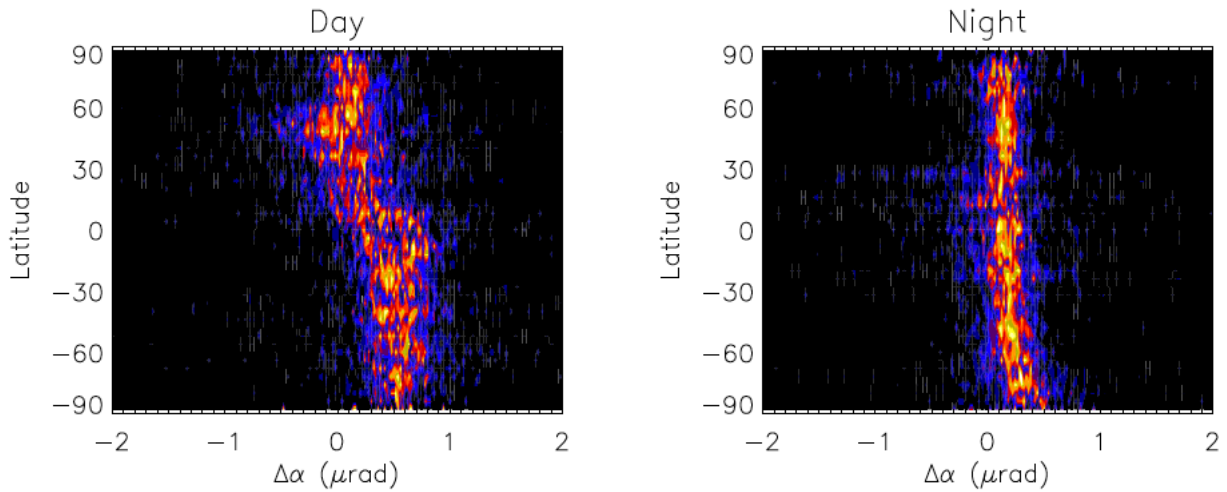
Fig.8. As in Fig.5 for MetOp-B from Jan 2023. MetOp-C (not shown here) has very similar $\Delta\alpha$ PDFs to MetOp-B.
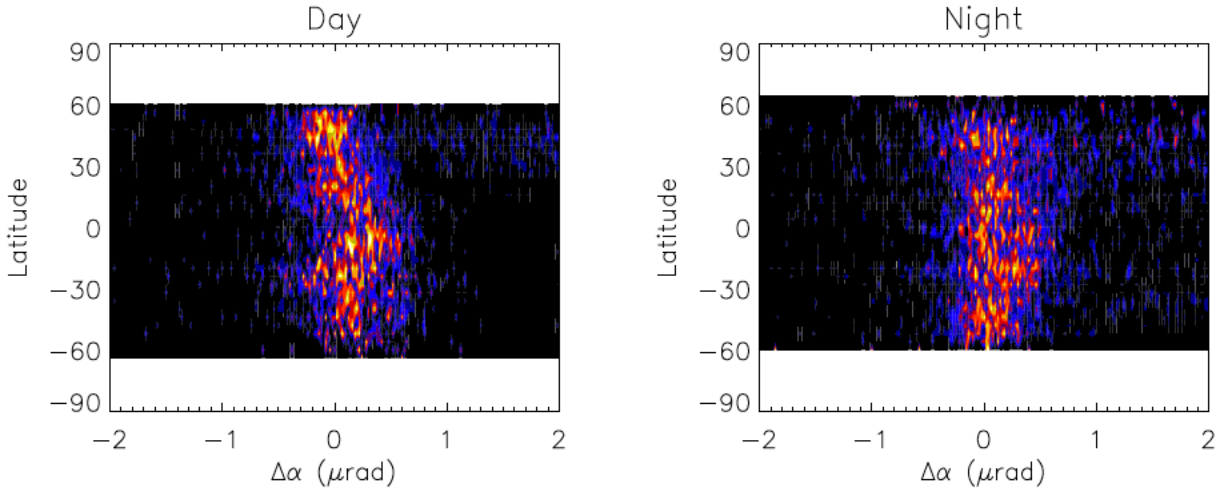
Fig.9 As in Fig.5 for FY3-E from Jan 2023.

3.2   Diurnal and Solar-Cycle Variations

The mean (μ) and standard deviation (σ) of $\Delta\alpha$ from January and July 2013 show a non-uniform distribution that varies with local solar time (LST), geographical location, season and solar activity [Figs. 10-11]. To illustrate the LST and latitudinal dependence, we used the COSMIC-1 measurements from January and July 2013 when solar activity was near its maximum. The monthly data are aggregated to 4° latitude and 2-h LST bins, using the quality screening criteria as shown in Table 1 with QC#4 and QC#5 (120 km). For the solar cycle variation, we used all COSMIC-1 data from 2006 to 2019 and averaged all-LST to produce a time series of monthly zonal mean. During most part of its mission (2007-2017), COSMIC-1 had a full diurnal sampling from its 6-satellite constellation on a precessing orbit. But in the later period, failure of some satellites degraded the diurnal sampling and yield a slightly noisy result in the time series.

There are significant differences between the $\Delta\alpha$ morphologies derived from the $d\phi_{ex}/dh_t$ method [Figs.10-11] and the κ method [Fig.12]. The $d\phi_{ex}/dh_t$ method reveals both negative and positive values in the $\Delta\alpha$ distributions, showing mostly negative during the daytime and positive at night. The κ-method always produces a negative RIE value from the product of a negative κ value and $(\Delta\alpha_1 - \Delta\alpha_2)^2$, regardless of day and night. To further illustrate their differences, we applied the same method (Eq.7) separately to the ϕ_{exL1} and ϕ_{exL2} data, and derived $\Delta\alpha_1 \equiv -d\phi_{exL1}/dh_t$ and $\Delta\alpha_2 \equiv -d\phi_{exL2}/dh_t$. Unlike the $(\Delta\alpha_1 - \Delta\alpha_2)^2$ distribution derived using an ionospheric electron density model [Angling et al., 2018], the $(\Delta\alpha_1 - \Delta\alpha_2)^2$ distributions and variations derived from the multi-year COSMIC-1 RO data [Fig.12] are more realistic, and they can be properly compared to the $\Delta\alpha$ morphology derived from the $d\phi_{exL2}/dh_t$ method.

Since the $(\Delta\alpha_1 - \Delta\alpha_2)^2$ distribution was introduced to provide a leading-order (f^{-2}) correction of the ionospheric impact on the radio wave propagation, it is expected that the higher-order and bending-independent RIEs may be not captured by the κ method. In other words, the distribution and variation of $\Delta\alpha_1 - \Delta\alpha_2$ difference cannot be fully characterized by

$(\Delta\alpha_1 - \Delta\alpha_2)^2$. For the evaluation of RIE impacts on temperature and humidity in the later section, $\Delta\alpha_1 - \Delta\alpha_2$ represents the persistent bias term in the inversion problem applied to the α data. As seen in Fig.10, not only two subtropical $\Delta\alpha$ peaks are negative during the daytime, but they also exhibit different mean values with a larger magnitude in the NH. This subtropical difference is much less pronounced in the $(\Delta\alpha_1 - \Delta\alpha_2)^2$ distribution [Fig.12]. In addition, the summer-winter contrast (January vs July) is more pronounced in the $\Delta\alpha$ distribution than in the $(\Delta\alpha_1 - \Delta\alpha_2)^2$ as used by the κ method. The seasonal and hemispheric differences between the $\Delta\alpha$ and $(\Delta\alpha_1 - \Delta\alpha_2)^2$ morphologies are reflected in their solar cycle variations as well. The κ-method correction with $(\Delta\alpha_1 - \Delta\alpha_2)^2$ shows a variation symmetric about the equator [Danzer et al., 2020], similar to the distribution revealed in Fig.12c. Thus, depending on how the RIE is derived, the application of two different RIE corrections as described above would likely have different impacts on the neutral atmospheric retrievals and the α data assimilation.

Solar-cycle variations are more pronounced in the daytime $\Delta\alpha$ than in the nighttime [Fig.11], as expected for the RIE associated with the photoionization in the ionosphere. The $\Delta\alpha$ time series derived from the $d\phi_{ex}/dh_t$ method shows a larger negative daytime RIE with a hemispheric asymmetry during the solar maximum years, but a larger positive nighttime RIE during the solar minimum years. At high latitudes, a summertime positive RIE appears to be a repeatable phenomenon with slightly higher values in the NH nighttime. There is an indication of weak solar-cycle variations in the daytime high-latitude $\Delta\alpha$. The solar cycle variations from COSMIC-1 are consistent with the MetOp-A/B/C observations (not shown), which have global coverage at two fixed LSTs. In summary, the solar-cycle variation of the RIE derived from the $d\phi_{ex}/dh_t$ method differs substantially from those from the κ-method based on $(\Delta\alpha_1 - \Delta\alpha_2)^2$. The time series of RIEs derived from the κ-method exhibits little high-latitude variation and has a similar daytime solar cycle in both NH and SH subtropics.

In addition to the mean (μ) distribution of $\Delta\alpha$, its spatiotemporal variability also plays an important role in the RIE correction. If the underlying processes are not randomly and vary nonlinearly with RIE, a spatial or temporal average may not eliminate the RIE impacts on the neutral atmosphere retrievals. Because the fast and nonlinear ionospheric processes may impact the RIE, we further characterize the $\Delta\alpha$ variation in terms of standard deviation (σ) on a monthly gridded map. In this calculation we compute the monthly μ and σ maps of $\Delta\alpha$ on a latitude x longitude (4°x8°) grid for every 2-h LST bin. Fig.10 shows the LST-and-latitude distributions of μ and σ from Jan and July 2013. Both variables exhibit a strong diurnal variation, which is latitude-dependent with a large σ amplitude at mid-latitudes and during the nighttime. The correlations between the μ and σ distributions are complicated, but in both months the σ amplitude can be greater than the $\Delta\alpha$ mean, particularly in the nighttime. The season-dependence of the σ diurnal variation shows a larger amplitude at mid-latitudes in the winter daytime/evening and in the summer nighttime.
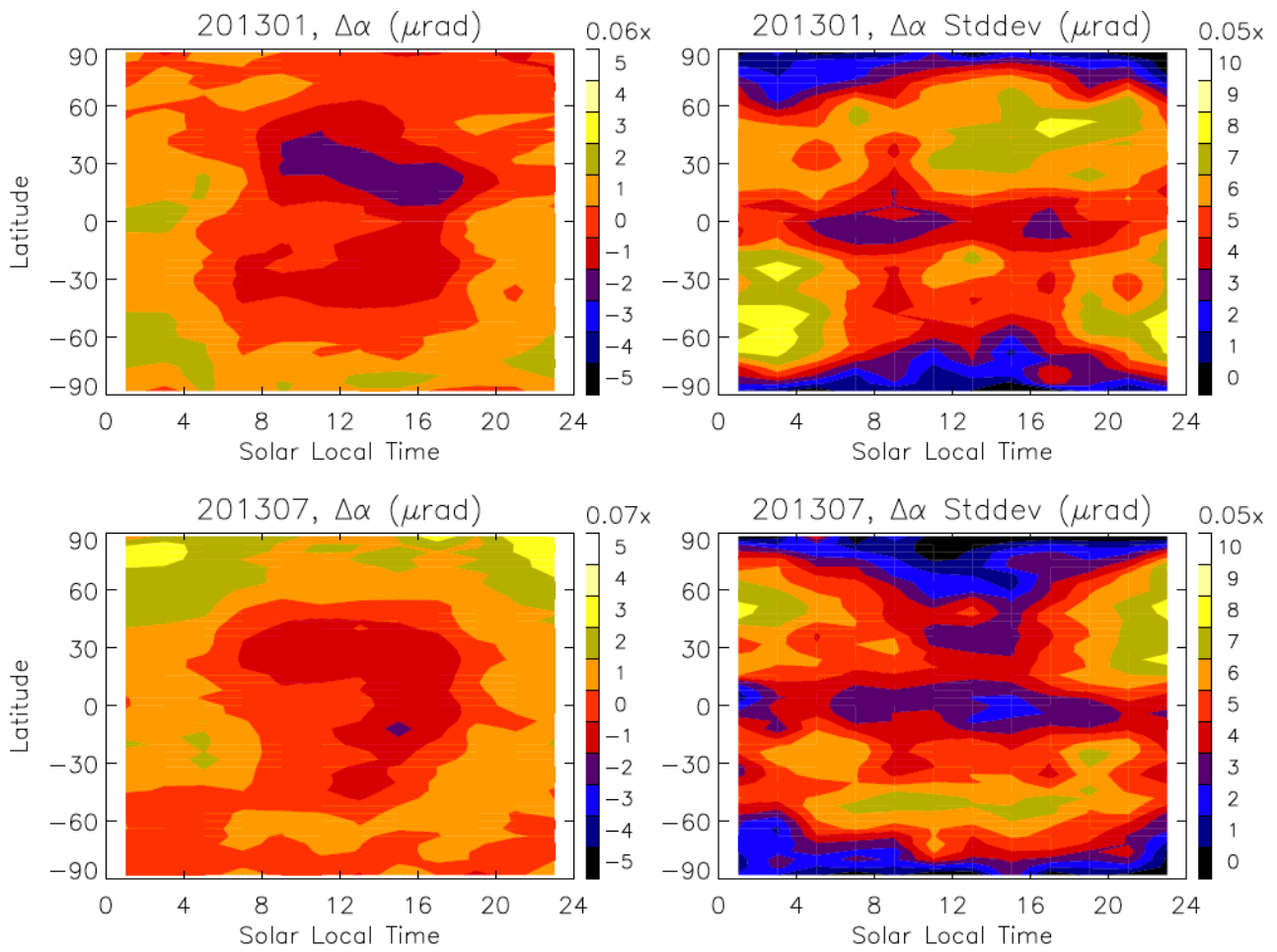
Fig.10. Latitude (4°-bin) and solar local time (2h-bin) dependence of COSMIC-1 RIE $\Delta\alpha$ mean (μ) and standard deviation (σ) from January and July 2013.
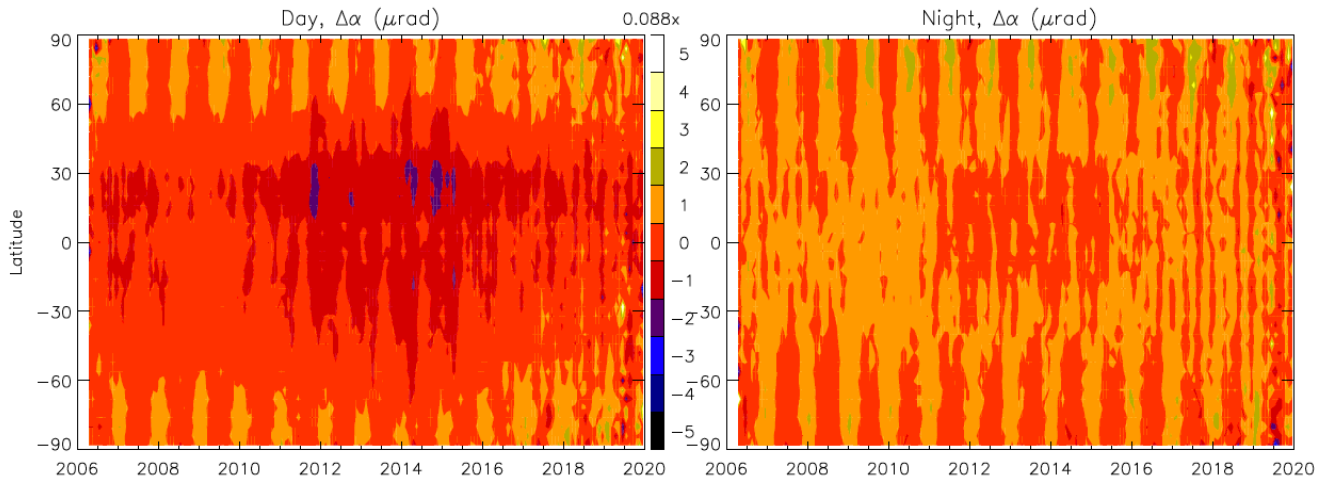
350

Fig.11. Long-term variations of the daytime and nighttime mean $\Delta\alpha$ from COSMIC-1 as a function of latitude during 2006-2020.
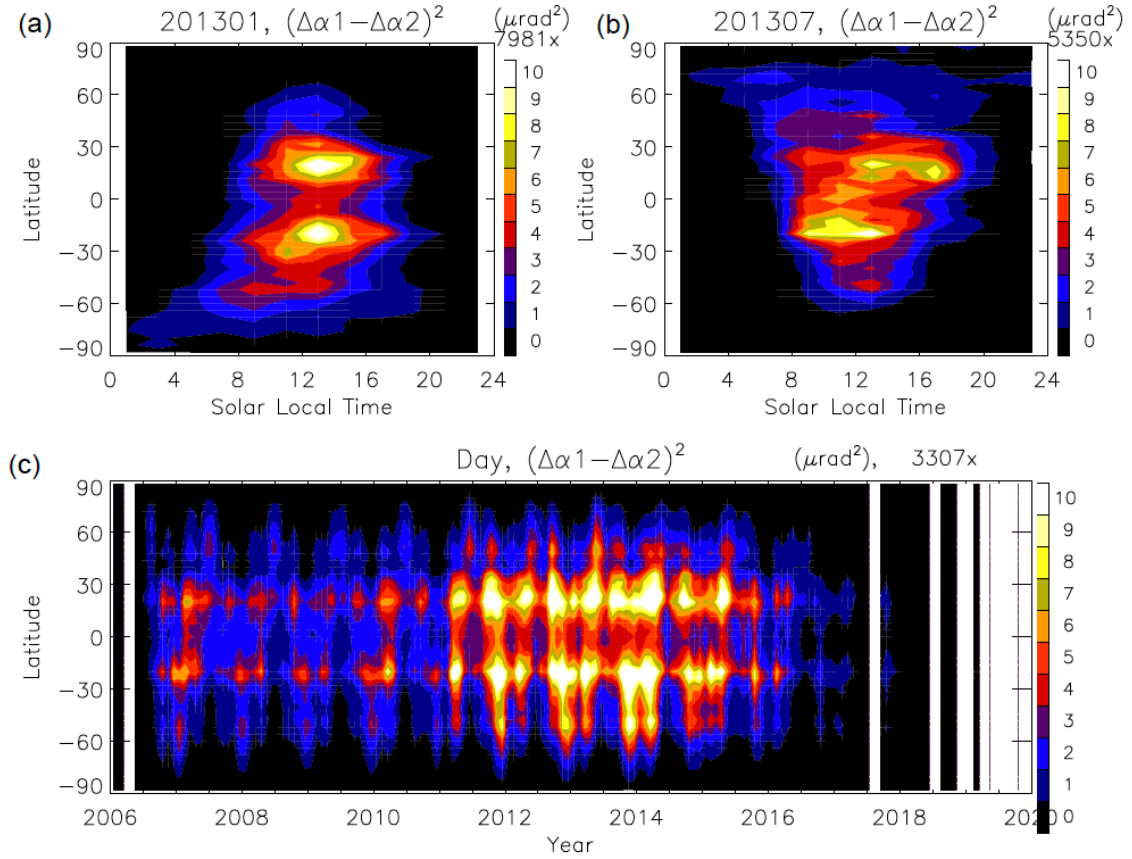
Fig.12. The $(\Delta\alpha_1 - \Delta\alpha_2)^2$ distribution and variations derived from the COSMIC-1 data using $\Delta\alpha_1 \equiv -d\phi_{exL1}/dh_t$ and $\Delta\alpha_2 \equiv -d\phi_{exL2}/dh_t$. The $(\Delta\alpha_1 - \Delta\alpha_2)^2$ distribution here can be compared to the RIE derived from the κ-method in Fig.10, by multiplying a κ value between -10 and -15 rad^{-1} for 60 km.

3.3 Longitudinal Variations and Dependence on Geomagnetic Field

It is well recognized in previous studies that ionospheric variability can be also driven by the atmospheric waves originated in the lower atmosphere and the geomagnetic forcing from above [Forbes et al., 2006; Immel et al., 2006]. The underlying ionospheric processes of RIEs are likely dependent on geomagnetic activity as well as on longitudinal and seasonal wave variability. Thus, it is important to quantify the $\Delta\alpha$ distribution and its variations in the geographical and geomagnetic coordinate systems. The monthly averaged geographical $\Delta\alpha$ maps derived from COSMIC-1 data for January and July 2013 show a large nighttime longitudinal variation in $\Delta\alpha$ [Fig.13], which may be induced by the atmospheric planetary waves forced in the lower atmosphere and mesosphere. There is also an indication that the daytime $\Delta\alpha$ distributions vary slightly with the geomagnetic field at low and middle latitudes in both seasons. At high latitudes, however, there is no any noticeable $\Delta\alpha$ variation and connection to the auroral activity in the polar caps. The dependence of RIE on the geomagnetic field variation is expected from the high-order ionospheric effect [Hoque and Jakowski, 2007], and such RIEs can be both positive and negative [Vergados and Pagiatakis, 2011].

It is interesting to note that the nighttime $\Delta\alpha$ distributions bear a strong resemblance to those derived for the Es climatology in summer and winter [Wu et al., 2005; Arras et al., 2009]. Previous studies showed that the occurrence of Es from global GNSS-RO observations tends to peak at 90-110 km altitudes near mid-latitudes during the summer months, and is strongly modulated by the solar diurnal and semidiurnal migrating tides. Syndergaard [2000] discussed the Es-induced morphology of RIE showing a frequent influence of Es below the occurrence altitude. This study also suggested the RIE correction scheme for the Es-induced errors.

However, it remains unclear to what extent Es may contribute to the RIE amplitude and variability. Although the $d\phi_{ex}/dh_t$ method attempts to minimize the Es impacts using more measurements from higher altitudes [Fig.2], the RIE maps from Fig.13 seem to indicate that Es may still have a significant role in the nighttime RIE variation. Because the E- and F-region ionospheric variabilities are driven by different processes, their contributions to the RIE would appear as different morphologies in terms of latitudinal, longitudinal and local time distributions. As elucidated by Syndergaard and Kirchengast [2022], path differences between the L1 and L2 propagation in a 3D structured ionosphere are the major cause of various RIEs, which can vary with the geomagnetic field and the spatial distribution and gradient of electron density. Depending on the relative importance of these contributors, the RIE corrections and impacts on the neutral atmospheric measurements are likely to differ from each other.
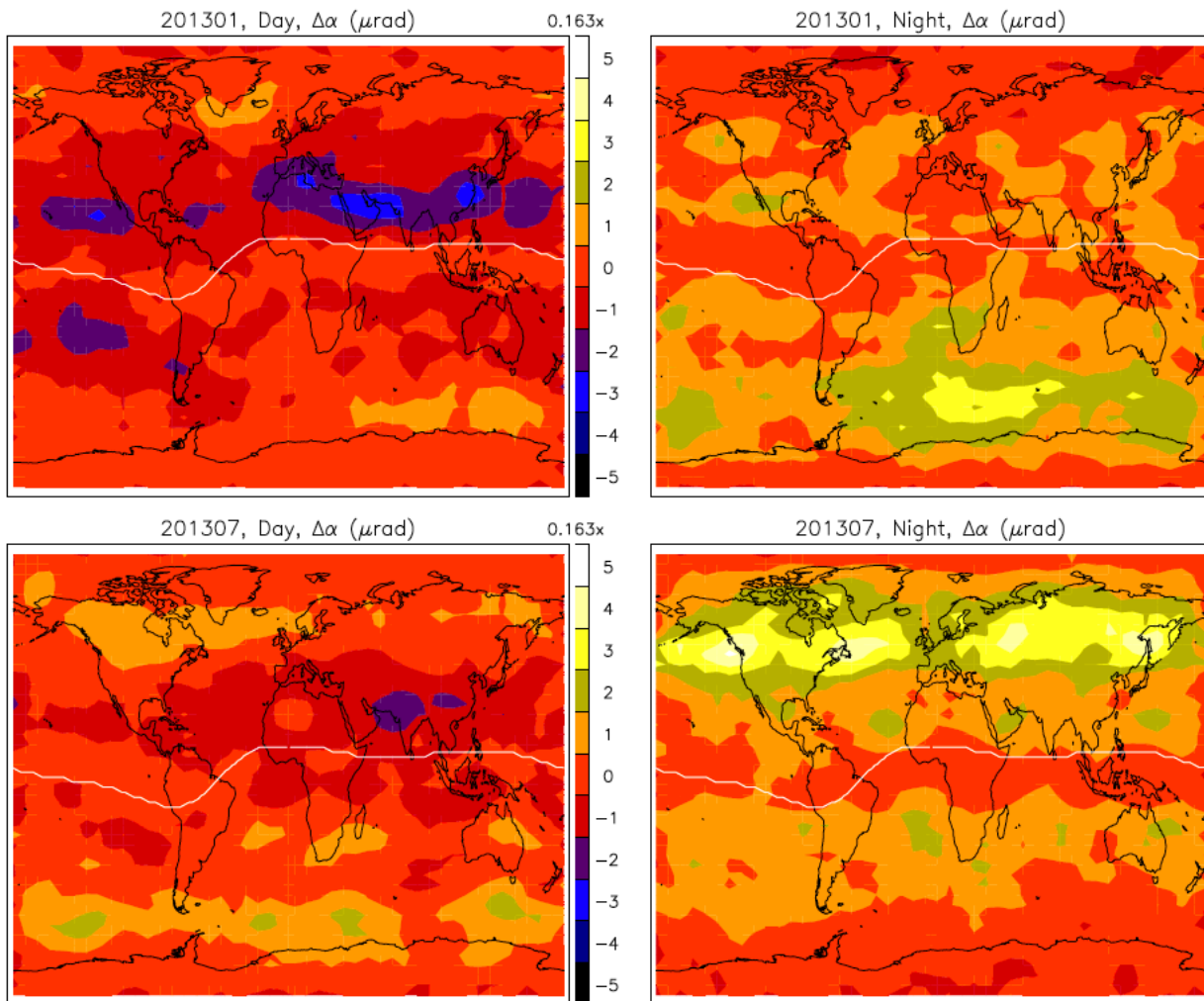
385   Fig.13. Geographical maps of the $\Delta\alpha$ derived from COSMIC-1 $-d\phi_{exL1}/dh_t$ measurements for January and July 2013; the white lines display positions of the geomagnetic equator.

4   RIE Impacts on Data Assimilation (DA)

4.1   Goddard Earth Observing System for Instrument Teams (GEOS-IT)

To quantify potential impacts of the observed $\Delta\alpha$ morphology on the neutral atmosphere, we conducted several data

390   assimilation   (DA)   experiments   using   the   GEOS-IT   DA   configuration   of   NASA   GMAO/GSFC
https://gmao.gsfc.nasa.gov/GMAO_products/GEOS-IT). GEOS-IT retains many characteristics of GEOS Forward Processing
System, including the spatial resolution (~50 km) and the use of a three-dimensional variational (3D-Var) DA algorithm, and
allows the instrument teams to benefit from many model enhancements of GEOS, leading to more realistic representations of

moisture, temperature, land surface, and analysis changes that introduce the most modern new satellite observations into the system. The GEOS-IT configuration employed in this study (GEOS-5.27 DA system) assimilates GNSS-RO α observations with a 6-hour update cycle [McCarty et al., 2016; Gelaro et al, 2017], using the RO forward operator as in the operational NCEP (National Centers for Environmental Prediction) bending angle method (NBAM) [Cucurull et al., 2013]. As shown in Cucurull et al. [2014], the GNSS-RO observations have both direct and indirect impacts on the quality and skills of analyses and forecasts of NWP systems. The RO assimilation results in a more accurate bias correction for infrared and microwave radiance measurements, and therefore leads to more effective use of satellite radiances by allowing more radiance data that satisfy the quality control requirement. This indirect impact has made the GNSS RO observation more valuable even the number of profiles is relatively small compared the radiance measurements. Because the GNSS-RO technique is essentially traced to the SI length unit, with little dependence on radiometric calibration, it serves as an anchor of the radiance bias correction for the microwave and IR sounders.

The direct impact of RO data comes from their α sensitivity to the temperature in the upper troposphere and stratosphere. The RO measurements help to constrain the temperatures at 8-40 km in all-weather conditions with the global and full local time coverage. As a measurement forward model, the ROPP package produces the α data and their errors from the ϕ_{ex} data [Healy et al., 2007; Cucurull et al., 2013, 2014; Zhang et al., 2022]. The GEOS DA algorithm for the RO observations assumes the zero α bias without RIE. As remarked in previous DA studies above ~30-40 km [Healy et al., 2007], the RIE correction schemes for the α data analysis is important and can affect the DA data quality if not implemented, such as those systematic α errors associated with the persistent influence of the ionospheric processes. Despite the effort to minimize the RIE impact by increasing RO measurement uncertainty at altitudes above 40 km, RIE impacts are still evident in the resulting analysis data [Danzer et al., 2013].

The RO observation data used in the DA impact study contain the data mostly from COSMIC-1 with a global distribution. The observation error used in the GEOS-IT DA is mostly identical to the NCEP system where the final observation errors are inflated at the super-obbing stage. The super-obbing is a technique to reduce redundant information in the observational data and the data density [Purser et al., 2000]. The observation error plays a key role in determining the weight between the model forecast and RO observations in the DA, which is a function of latitude and height. In the next section we introduce the ϕ_{ex}-based RIE correction scheme as described in Section 3 and carry out a set of DA experiments to quantify the impact of RO data with and without the RIE on the GEOS-IT DA products.

4.2   DA Experiments

To assess the RIE impacts on DA products, we performed the GEOS-IT experiments for the Dec-Jan of 2016/2017 using the values derived from the $d\phi_{ex}/dh_t$ method (Section 2.2). In this experiment period, about 2000 α profiles were analyzed per day from multiple GNSS-RO missions (i.e., GRACE, Metop-A, and COSMIC-1). The horizontal resolution of GEOS-IT analyses and forecasts is ~50 km, and results were archived at 72 model layers from the surface to ~1Pa (~80 km). Four DA experiments were conducted: (1) control (CTL) experiment that assimilate all RO observations assuming no RIE

bias; (2) GPS-denial (NoGPS) experiment by excluding all RO data; (3) constant bias (BiasM2) experiment by adding a large constant RIE ($\Delta\alpha$ = -2 µrad) to all RO data; and (4) the $d\phi_{ex}/dh_t$ derived bias experiment (BiasLST) by incorporating the latitude-LST dependent RIE in α that is similar to the COSMIC-1 observation as shown in Fig.14.

430   The month of December 2016 was used to spin up the GEOS-IT analysis-forecast system, and the RO data were injected starting from January 1 2017 for the RIE-impact experiments. The objective of these experiments is to quantify the potential impacts of the RIE bias from assimilating the α data with the recent upgrades of the GEOS-IT system (model and DA algorithms). We compared the Jan 1-10 GEOS-IT analyses by differencing each experiment from CTL for the zonal mean temperatures as well as for hourly means in the middle and upper atmosphere. The importance of RIE impacts depends on the

435   RIE amplitude relative to atmospheric variability at each altitude and how much the GNSS-RO measurements are weighted in the DA system. The GEOS-IT α measurement error covariance matrix used in all DA experiments is identical to the normal RO data assimilation. The α error covariance matrix was designed to reduce the weighting on the RO α data at higher altitudes so that their errors there does not impact the lower atmosphere significantly. Nevertheless, the DA results from the α data with a RIE can still have non-negligible impacts on the DA data in the middle atmosphere.

440
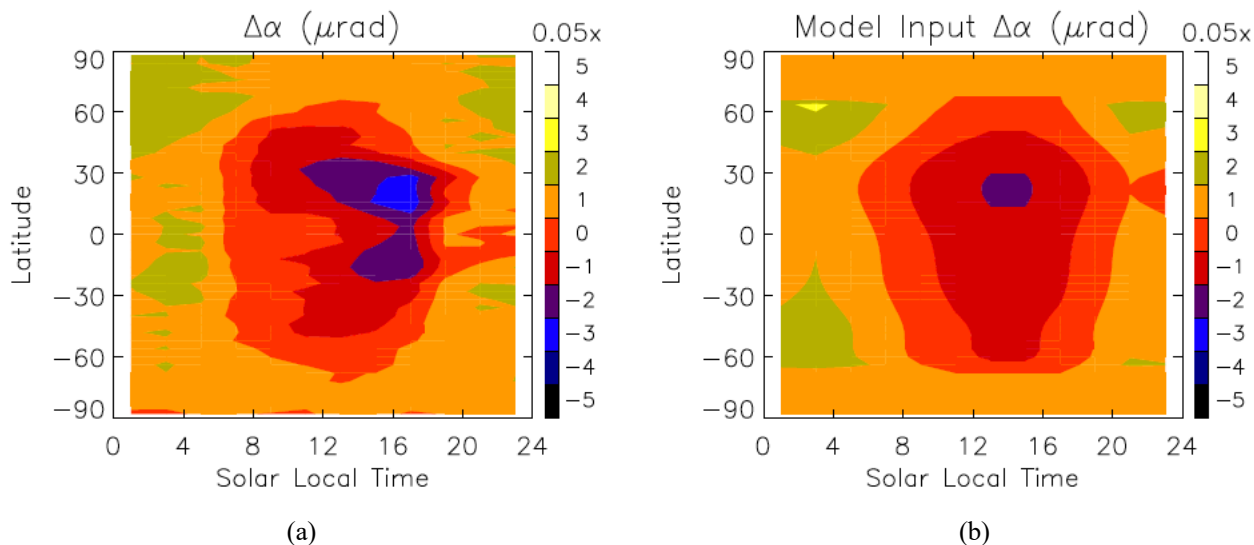
Fig.14. (a) Annual mean $\Delta\alpha$ variations derived from 2013 COSMIC-1 data; (b) Parameterized $\Delta\alpha$ variations used as the RIE input for the "BiasLST" DA experiment.

445   **4.3   RIE Impacts on Temperature**

The RIE impacts on the DA results tend to grow with time and height in amplitude, despite the reduced sensitivity to the RO α measurement in the upper atmosphere. We chose the 5-7 day period after the GPS measurements are injected with a bias or denial, to characterize an accumulated impact from the spatiotemporal growth of the DA system. During the initial growth period (0-5 days), the DA system continues to inject the biased/denied RO data and the rate of growth between CTR

and other perturbed runs appears to be large. The growth rate of differences slows down on days 5-7, which yields a better characterization of the RIE impacts.

The 3-day (Jan 5-7) averaged temperature differences between the CTL and the perturbed experiments (NoGPS, BiasM2, and BiasLST) show significant GPS and RIE impacts on the GEOS-IT analyses (Figs 15-17). The zonal mean differences (Fig. 15) display the most prominent impacts at high latitudes in the upper stratosphere (above ~30km). Compared to the NoGPS impacts (Fig.15a), the GNSS-RO data with an unrealistically large (2 μrad) bias (Fig.15b) appear to do more harm than good for the DA, showing a bias of 3-30 K in the upper atmosphere and 0.3-0.6 K in the troposphere. The large biases in the upper atmosphere suggest that the DA system trusts the GNSS-RO measurements with the accuracy better than 2 μrad at these altitudes. In the BiasLST case where the RIE input uses a more realistic value (~0.05 μrad) during the daytime, the RIE impact reduces to ~1-3 K in the upper stratosphere. The magnitudes of temperature error introduced by this RIE specification (Fig. 14) are comparable to the results reported by Danzer et al. [2020] from the κ-method.

In the lower troposphere the GNSS-RO contribution to the DA comes primarily from an indirect impact in which the RO data help to correct the radiance bias between microwave and infrared sounders and allow more radiance data to be assimilated [Healy et al., 2005; Cucurull et al., 2014]. The CTL-NoGPS differences (Fig 15b) show that the impacts of GNSS-RO data are mostly in the polar regions with a temperature improvement of ~0.3-0.9 K. These impacts extend to the lowermost of the polar atmosphere. The large RIE bias (BiasM2, Fig 15d) has a comparable (0.3-0.6 K) impact on the lower polar atmosphere. For the realistic RIE bias (BiasLST), the impacts are mostly small (<0.3 K) in the lower troposphere.

It is interesting to observe that the GNSS-RO impacts largely reside in the high latitude polar regions, which appears to be the case for the denial (NoGPS) and perturbed experiments. These results are consistent with some of the earlier studies with RO-denial experiments, showing a larger impact at higher latitudes [Bonavita, 2014; Cucurull and Anthes, 2015]. It is worth pointing out that the large impacts in the polar region occur from day 1 (not shown) when the RO data is injected and exhibit the similar magnitude throughout the entire January experiment period. Although the sign of RIE-induced biases may change with time, as seen in planetary wave progression, the largest RIE amplitudes always reside at high latitudes. Because direct and indirect impacts from the GNSS-RO observations may act collectively in the DA output [Healy et al., 2005], these DA experiments seem to indicate that in the RIE impacts might larger in the region where wave activity is stronger.

In the upper atmosphere where the solar migrating tides become dynamically dominant, the impact of diurnally-varying RIEs on these processes needs to be quantified globally. As detailed in Appendix B, the local-time-dependent RIE (BiasLST), despite of inducing a mean temperature bias in the mesosphere, does not produce significantly large impacts on the tidal amplitudes there since these waves are locked in phase to the solar forcings from the troposphere and stratosphere.

Whole Atmosphere	Troposphere and Lower Stratosphere
(a) CTL - NoGPS	
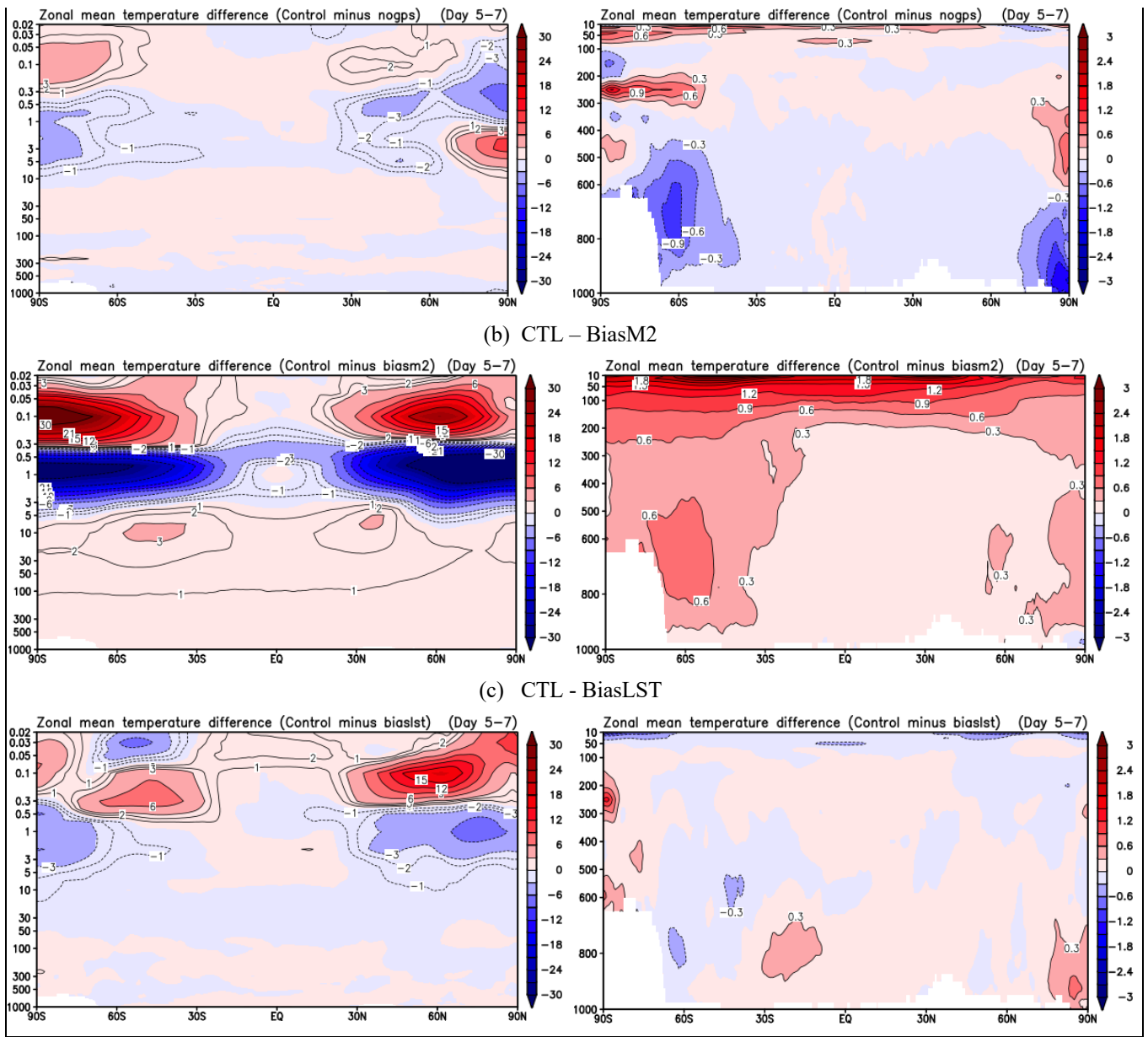
480

Fig.15. The zonal mean temperature differences between controlled and perturbed experiments. A different color scale is used for the lower atmosphere, to highlight small values in this region.

5   Discussions

5.1   Negative and Positive RIE Values

485   Causes of RIE are complex because of higher-order effects on the refractive index and effects of the propagation path difference between two frequency bands. Collectively, these effects can induce an RIE from the dual-frequency method, if the radio wave propagation through a structured and anisotropic ionosphere [e.g., Davies, 1965; Kindervatter and Teixeira, 2022]. Brunner and Gu [1991] modeled the higher order terms from the series expansion of the refractive index, including the second-order effect from the path difference between the L1 and L2 frequencies and the third-order effect from the geomagnetic field.

490   While the second-order RIEs are mostly negative, the third-order RIEs can be both positive and negative. To quantify the RIE for ground-based receivers, Hoque and Jakowski [2007] developed a correction algorithm that can be applied to real-time GNSS applications and reduce the higher-order phase errors.

In the GNSS-RO applications, studies have also found that the second-order RIEs are mostly negative [Liu et al., 2013] and the third-order could have both positive and negative values in α and refractive bias depending on the viewing geometry

495   with respect to the geomagnetic field [Vergados and Pagiatakis, 2011; Qu et al., 2015; Li et al., 2020]. These model simulations all suggested a relatively small RIE value that is typically less than 0.1 µrad, generally smaller than what was observed with the $d\phi_{ex}/dh_t$ method introduced in Sections 2 and 3. Nevertheless, the positive and negative $\Delta\alpha$ values seen in Figs. 5-9 suggest that the first and second-order RIE effects are equally important. Examining the mean deviation between CHAMP and COSMIC-1 α and a climatology model at 60–80 km altitudes, Li et al. [2020] also reported positive and negative values of

500   RIE, showing larger negative RIEs in the daytime and relatively smaller positive RIEs at night as seen in Fig.10. Note that this study did not use any climatology model for α, and the $d\phi_{ex}/dh_t$ method is self-sufficient with an empirical linear fitting to each individual profile. In summary, compared to the idealized model simulations, the large variability in the observed positive and negative $\Delta\alpha$ reflects the complex nature of RIEs in the dynamical ionosphere.

5.2   Impacts of Es and RO Top Height

505   An Es layer can produce large RIEs near the layer heights with a long tail extended to lower tangent heights in the GNSS-RO profile [Syndergaard, 2000; Syndergaard and Kirchengast 2022]. If the RO measurements stop at or below the Es layer, the $d\phi_{ex}/dh_t$ method can be significantly affected by the Es tail and lead to an overestimated RIE. In some GNSS-RO operations (e.g., MetOp), the top of RO data acquisition is often capped at ~85 km. To quantify effects from this low RO top height, we took advantage of the experimental MetOp-A data on 2020d161-2020d254 (June 9-September 10, 2020) when the

510   high-rate (100 Hz) GNSS-RO acquisition reached up to ~290 km. This data set allows us to quantify the RO top impact from different truncation heights.

In this comparative analysis, the $d\phi_{ex}/dh_t$ method was applied to the same experimental MetOp-A data from June 9-September 10, 2020, but from different RO truncation tops: 90, 120 and 170 km. The 90-km truncation represents some missions before 2020 such as MetOp and SACC when the high-rate RO data acquisition stopped at ~85 km. The 120-km

515 truncation height have been adopted by several missions (e.g., COSMIC-1, TSX, FY3), whereas the 170-km top operation corresponds to some of the recent commercial GNSS-RO constellations (e.g., Spire and PlanetiQ). More detailed information on the RO sampling parameters of the past and current GNSS-RO missions can be found in Appendix A.
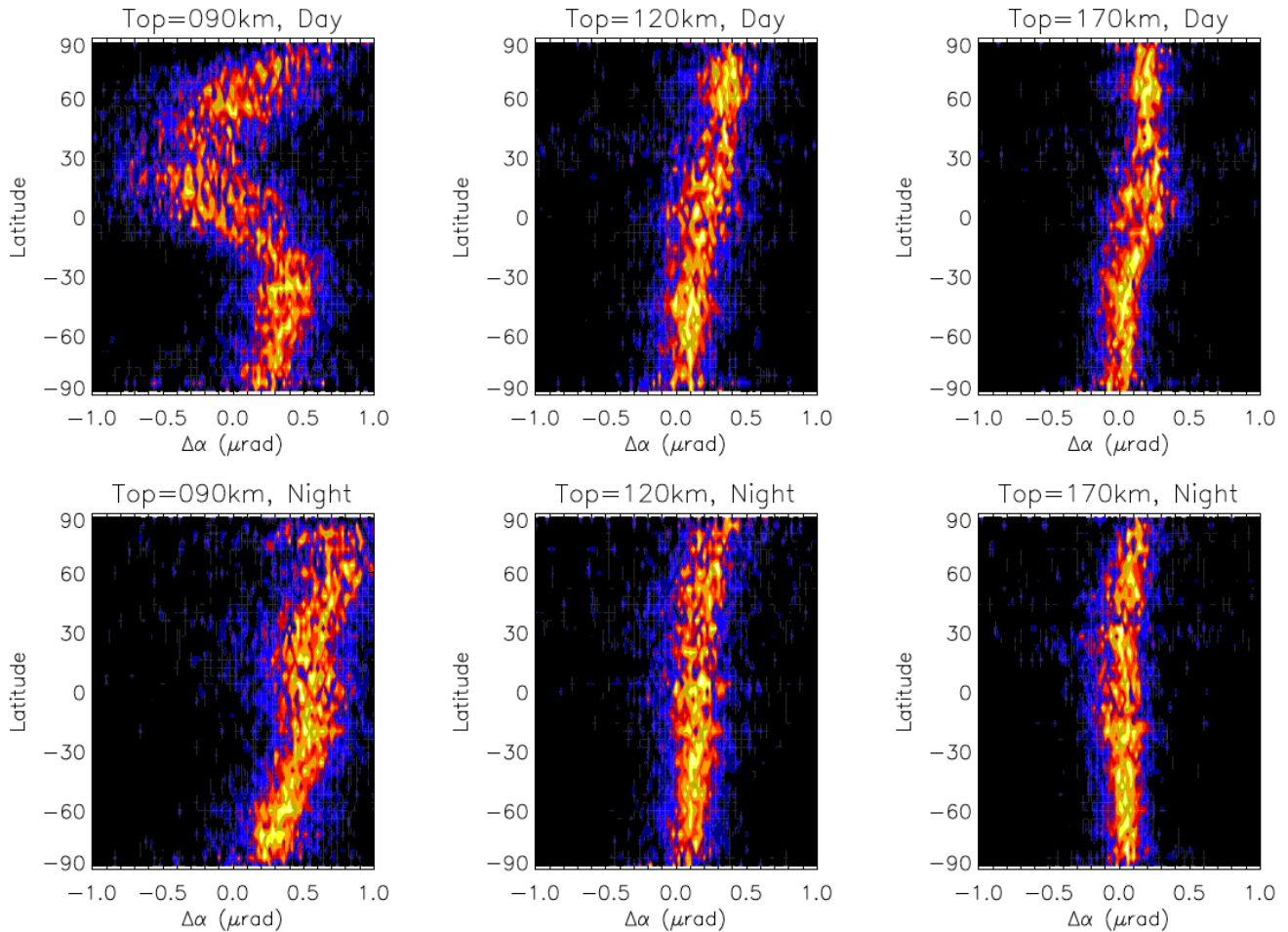
Fig.16. Probability distribution function (PDF) of the RIE derived from the $-d\phi_{ex}/dh_t$ algorithm to compare impacts of the
520 RO top height truncation. The experimental data from the MetOp-A special scan during D161-D254 in 2020 were used in the analysis and the RIE statistics from day (top panels) and night (bottom panels) are reported separately. The RIE results from three RO cutoff top heights, 90, 120, and 170 km, are selected for comparisons.

As suggested by the results in Fig.16, it is imperative to raise the RO sounding top to at least 120 km for the RIE estimation, because the lower truncation height (90 km) exhibits an inconsistent RIE distribution from those obtained with a
525 higher truncation heights. The RIEs derived from the 120-km and 170-km truncations have similar statistics for both day and night, suggesting that the 120-km truncation would be high enough to overcome the potential Es influence on the RIE calculation. As shown in Fig.2c, the $d\phi_{ex}/dh_t$ method would suffer from the Es tail below the Es layers. By providing a few

RO measurements above the Es layer, it would help substantially to constrain $d\phi_{ex}/dh_t$ for the RIE calculation. Therefore, the inconsistent statistics from the 90-km truncation, compared to those derived from a higher RO top, can be explained primarily as the Es impacts. If one plans to use the $d\phi_{ex}/dh_t$ method to estimate and correct the RIE, the RO top height as summarized in Appendix C becomes an important parameter to know for the current and past missions.

5.3 RIE from Other Methods

5.3.1 Deviation from the Exponential Profile

RIEs and their effects can be evaluated with other methods or comparative analyses by including an α bias against ground-based radar observations [Danzer et al., 2013] and α climatologies [Li et al., 2020]. Here, we introduce a method that uses the height variation of the excess phase ϕ_{ex} profile in the upper stratosphere, to compare it with the expected exponential lapse rate. Since α is related to the $d\phi_{ex}/dh_t$ [Eq.6], the ϕ_{ex} profile contains information on the RIEs seen in α. It is shown in Melbourne et al. [1994] and Wu et al. [2022] that the iono-free ϕ_{ex} profile is proportional to

$$\phi_{ex}(h_t) \approx 1.8 \times 10^{-5} \cdot N(h_t)\sqrt{H \cdot R_e} \tag{8}$$

where N is atmospheric refractivity, H is the atmospheric scale height, and R_e is Earth radius. Because the refractivity is proportional to air density, it tends to decrease exponentially with height, $N(h_t) = N_0 e^{-(h_t-h_0)/H}$, from a reference N_0 at height h_0. Hence, a departure from the exponential height dependence as described by Eq.(8) may be used to evaluate an RIE in the ϕ_{ex} profile.

Several lapse rate comparisons are shown in Fig.17 where the ϕ_{ex} profile differences are highlighted in percentage from an exponential fit at heights above 40 km. The exponential model uses the data at 40-45 km for the fitting and extrapolate the model to the heights above and below. The model assumes a constant scale height at these altitudes, which may cause some errors if atmospheric temperature varies by 10-20%. However, any large percentage departures would raise a concern and might indicate a RIE in the ϕ_{ex} profile. Since Eq.(5) cannot completely remove the ionospheric contribution, the departure from the exponential can be used to better the nature of these RIEs. As discussed above, ionospheric multipaths and horizontal/vertical gradients might play a significant role in the RIE of the ϕ_{ex} measurements.

Fig.17a is a typical case where the exponential model fits well to the ϕ_{ex} profile up to ~50 km but exhibits negative biases (observation minus model) at higher altitudes. These biases can be as high as 40-50% at 50-60 km, much greater than 10-20% typically seen at lower altitudes. It is possible that the low biases were caused by a colder atmosphere at higher altitudes compared to the temperature at 40-45 km, because the scale height H is proportional to temperature and ϕ_{ex} is proportional to $\sqrt{H} \cdot e^{-(h_t-h_0)/H}$ in Eq.8. For example, to explain a 40% decrease in ϕ_{ex}, it would require that temperature drops from 270 K at 45 km to 210 K at 55 km, which might be feasible from a very strong gravity wave.

Fig.17b illustrates a likely ionospheric effect where a sharp thin layer at ~53 km creates a large disruption in terms of exponential dependence of ϕ_{ex} with height. Not only the height dependence of ϕ_{ex} does not obey the normal exponential decrease as expected from the neutral atmosphere, but also the departure from the exponential above the layer is severely lower

560   by more than 50%. It remains unclear why the layer disrupts more at heights above than below. In other words, if such behaviour is representative for the ionospheric effects of thin layers (e.g., Es), their RIEs on the neutral atmospheric measurements might be small.

       Fig.17c shows very different exponential dependences between the atmosphere below 40 km and above. To explain the 70% difference using Eq.8, one would have to assume a temperature difference of 120 K between 25 km and 45 km. On
565   the other hand, if a reference from the lower altitudes (e.g., 30 km) were used, it could help to reduce the biases in the lower atmosphere but would induce a much larger (> 100%) bias at higher altitudes. In summary, this is a case likely caused by a RIE that can a large departure of the ϕ_{ex} measurement from the expected exponential dependence with height. The biases above and below 40 km are too large to be explained by a normal atmosphere, but a RIE in the ϕ_{ex} measurement can certainly induce a large error like this.

570   Fig.17d displays a wave-like oscillation above 40 km in the bias from the exponential dependence. It perhaps reveals a real atmospheric gravity wave in the ϕ_{ex} measurement up to 60 km. If no RIE had impacted this profile, it would imply that the RO technique could provide good sensitivity to atmospheric temperature up to 60 km. Because RIEs can produce a local impact at a narrow height range like Es as well as an extended impact from the multipath propagation through the F-region, it remains a great challenge to distinguish between good cases like Fig.20d and RIE-impacted case like Fig.20b.

575

(a)   (b)

(c)   (d)
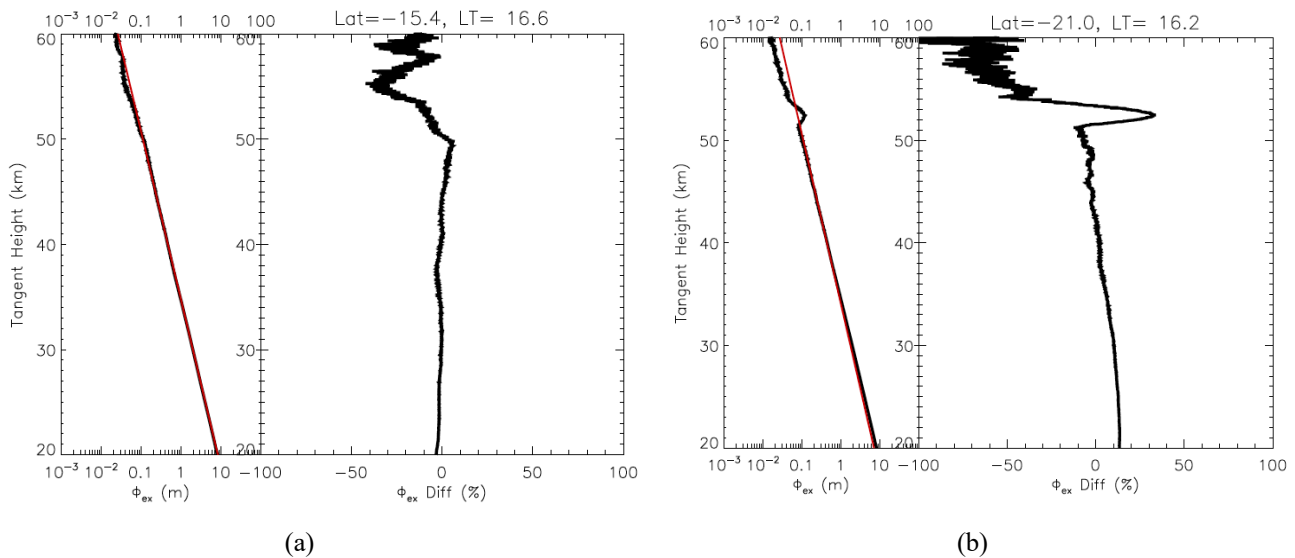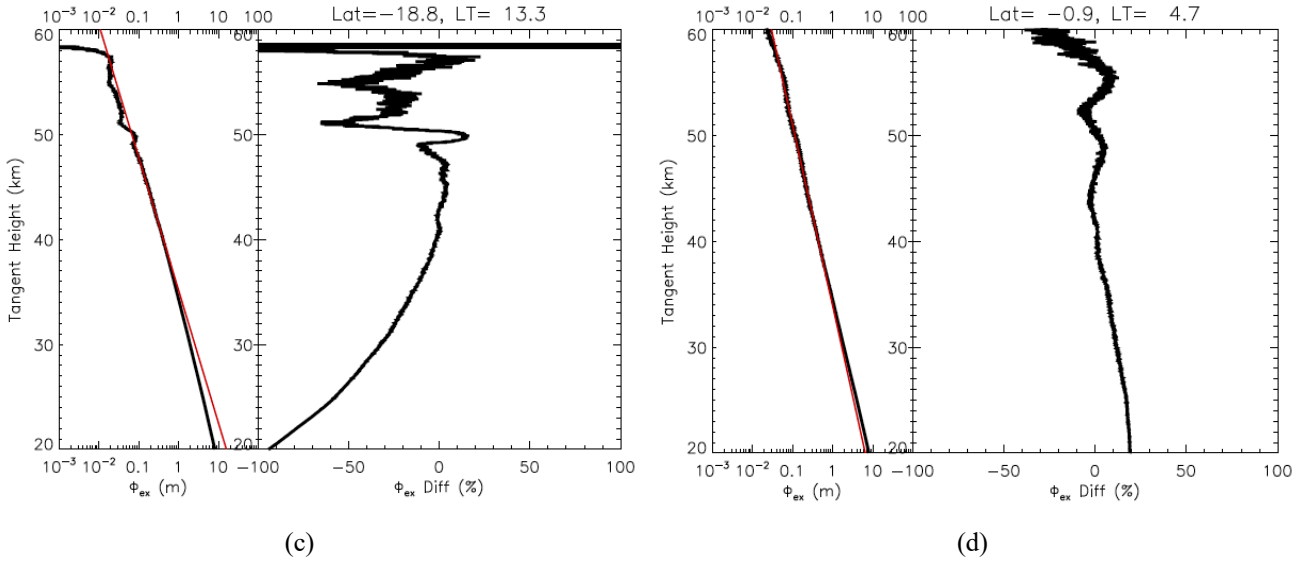
Fig.17. Examples of the departure of excess phase (ϕ_{ex}) measurements from an exponential fit (red line) at 40-45 km heights. The percentage difference between the observed and modelled ϕ_{ex} profile is displayed on the right as a function of tangent height. Selected cases are: (a) Typical negative departure from the exponential fit at higher altitudes; (b) Departure from the exponential function due to a layered structure near 52-53 km; (c) Largely different exponential dependence at heights above and below 40 km; and (d) Wave-like oscillations at high altitudes. These cases were extracted from COSMIC-2 observations on January 1, 2022.

5.3.2 Small-Scale Temperature Variances

Variability of the GNSS-RO temperature profiles can also be used to infer potential RIE impacts, because additional fluctuations induced by RIEs can be as large as the RIE-induced bias. As shown in Fig.10, the standard deviation of RIE $\Delta\alpha$ are often greater the mean, suggesting that these RIE $\Delta\alpha$ variations might have propagated to the atmospheric temperature retrieval. Because ionospheric variability has a wide range of spatiotemporal scales (e.g., scintillation, Es), it is possible that small-scale RIE $\Delta\alpha$ variations may be not completely removed and result in artificial wave-like oscillations in the retrieved temperature profiles.

To evaluate RIE impacts on RO retrieval variability, we analyzed the entire MetOp-A/B/C record of temperature data produced by the Radio Occultation Meteorology Satellite Application Facility (ROM SAF) to extract small-scale variances using the algorithm developed previously for Es and gravity wave (GW) studies [Wu et al., 2005; Wu 2006]. This algorithm is similar to those used in other studies [e.g., Tsuda et al., 2000; Schmidt et al., 2008], except that we derived GW variances using a bandpass filter for a more careful treatment on the measurement noise. In the data analysis with this algorithm, each RO temperature profile $T(z)$ is first processed with a running-window smoothing (truncation length Δz) to obtain a background ($\overline{T(z)}$). The difference $T(z) - \overline{T(z)}$) is used to compute the variance for this truncation Δz. The minimum

truncation length is defined by the 3-point length in the temperature retrieval, which is ~100 m in the upper troposphere and

600 stratosphere and can be used to estimate the measurement noise on a profile-by-profile. The bandpass-filtered variance is defined as the variance difference between the Δz and the 3-point truncation. The bandpass-filter method has been successfully applied to other satellite measurements for GW studies [Wu and Eckermann, 2008; Gong et al., 2012].
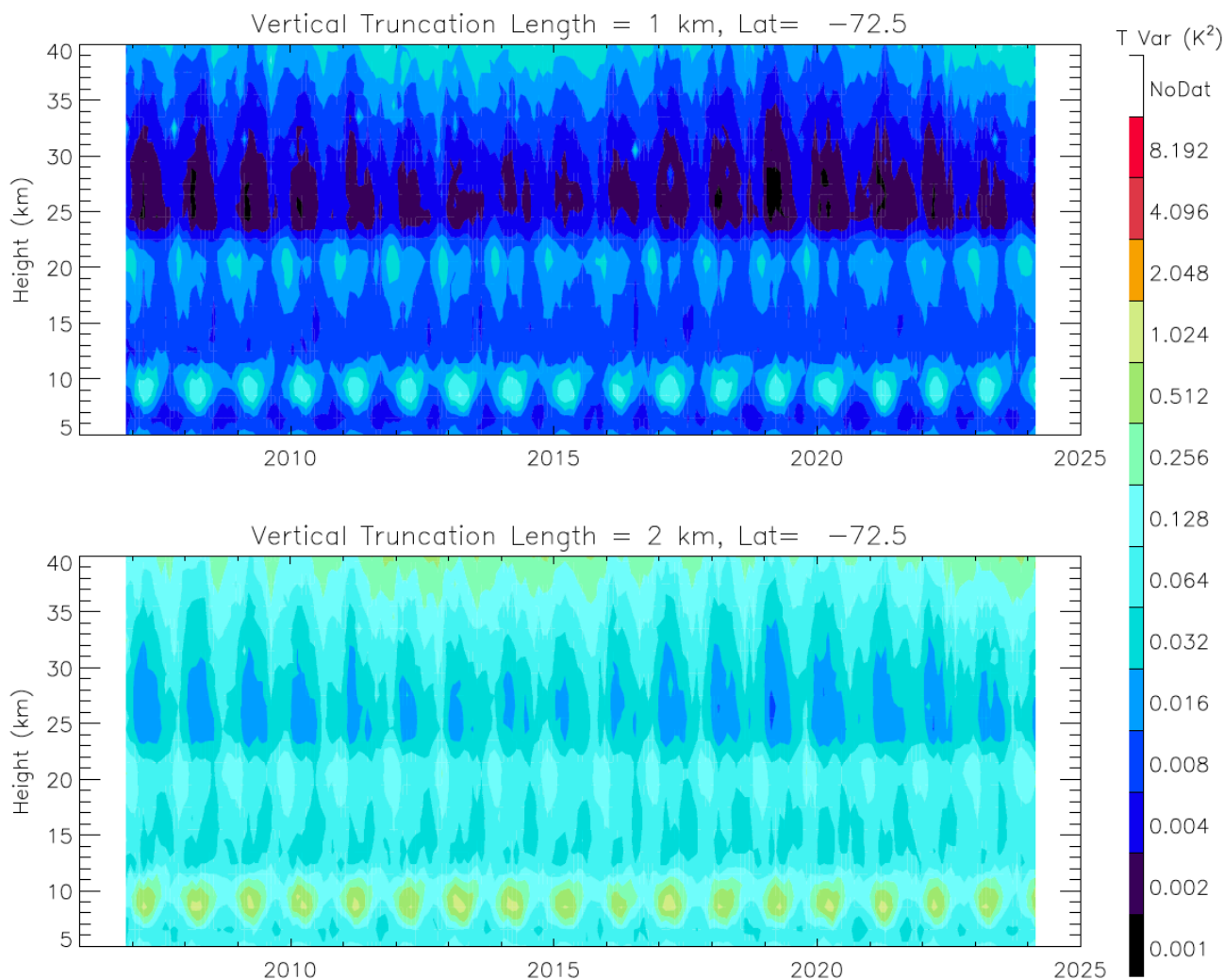
Fig.18. Time-height variation of the monthly small-scale variances derived from Metop-A/B/C RO dry temperature retrievals

605 at 72.5°S.

Fig.18 shows a time series of monthly MetOp temperature variances derived with the bandpass-filter method for truncations 1 km and 2 km at 72.5°S. A significant solar-cycle variation is evident in the temperature variances, particularly in the upper stratosphere, which suggest that RIE impacts might have an amplitude of 0.03 K^2 and 0.3 K^2 in the 1-km and 2-km variances at ~40 km altitude. The similar solar-cycle variation exists in the northern high latitudes (not shown) with a

610 comparable amplitude, but the solar-cycle dependence becomes less pronounced at low latitudes. It is expected that the RIE impacts would be greater at high latitudes, as revealed in the DA impact study (section 4.3). Although the solar-cycle-dependent temperature variations do not provide a direct indication on whether the RO temperature is artificially biased by a solar cycle influence, the earlier studies have found such bias evidence [Danzer et al., 2013; Li et al., 2020].

6   Conclusions

615   In this study we developed an empirical algorithm to estimate the RO residual ionospheric error (RIE) from the vertical gradient of excess phase (ϕ_{ex}) measurements at $h_t > 65$ km. The method, called the $d\phi_{ex}/dh_t$ method, is self-sufficient and based on the empirical linear fit to the ϕ_{ex} data on a profile-by-profile base. The RIE estimation does not rely on any auxiliary data or model sources. $d\phi_{ex}/dh_t$ is a good measure of α at high h_t (if there is a bending), but it also contains errors induced by other factors from the radio wave propagation in an inhomogeneous ionosphere such as higher-order 620 frequency dependence. The derived RIE is extrapolated to the RO measurements at the lower h_t, assuming that the entire α profile is impacted by error $\Delta\alpha$.

Although the derived RIE ($\Delta\alpha$) is dominated by positive values, the $d\phi_{ex}/dh_t$ method also produces negative values for both day and night. This is fundamentally different from the κ-method that only produces a positive RIE. Diurnal variations of the RIE $\Delta\alpha$ are latitude-and-LST dependent with larger negative amplitudes (up to -3 μrad) in the daytime tropics and 625 subtropics. The standard deviations of RIE $\Delta\alpha$ can be greater than their mean values in the climatology averaged by LST and latitude. Significant solar-cycle and longitudinal variations are found in the RIE $\Delta\alpha$ derived from observations. The dependence of RIE on geomagnetic field is evident but relatively weak, compared to the diurnal and geographical variabilities.

RIE impacts on data assimilation (DA) were evaluated with the experiments using the NASA GMAO Goddard Earth Observing System (GEOS) that assimilate GNSS RO α data for MERRA-2. A LST-latitude varying $\Delta\alpha$ bias similar to the 630 COSMIC-1 RIE climatology was added to the RO data in the GEOS-IT DA experiments. The RIE impacts on the DA temperature were found mostly in the polar stratosphere with a bias as large as 2-4 K at 1 hPa and ~1 K at 10 hPa. There is a small (±0.3 K) temperature bias in the troposphere. The diurnally varying RIE does not appear to impact on the migrating tides in the upper stratosphere and mesosphere, because the tidal waves are locked to the solar forcings from the lower atmosphere.

The $d\phi_{ex}/dh_t$ method requires the RO profile to reach at least 120 km to minimize the sporadic-E (Es) layer 635 influences. Es occurs mostly at 90-110 km with a strong localized effect in this altitude range, but its tailing effect can extend far below the Es layers in the RO ϕ_{ex} profile. Additional constraints from the RO measurements at 120 km and above would help to suppress the Es influences and provide a more accurate estimate of the RIE from the F-region ionosphere.

RIEs were also found in the RO ϕ_{ex} measurements by comparing the observed profile with an expected exponential decrease with height. In addition, the RIE impacts can be seen in the small-scale variance of RO temperature retrievals. In both 640 cases, the RIE amplitudes appear to increase with height and become a significant source of error in the upper stratosphere.

The findings from this study further emphasize the needs to treat RIEs carefully, especially with the growing infusion of commercial GNSS-RO data for climate studies.

Appendices

A. Bending Delay and Phase Advance

The radio wave propagation in GNSS-RO can have an excess phase ϕ_{ex} from both bending delay and phase advance. These opposite effects in ϕ_{ex} is often confused in the literature because they both have the same first-order dependence on f^{-2}. The bending effect increases the propagation pathlength and induce a delay in the excess phase measurements (ϕ_{exL1} or ϕ_{exL2}) because of the group velocity of radio wave. Although the group velocity is equal or less than the light speed, the phase velocity of radio wave propagation in plasma can exceed the light speed, causing a phase advance in ϕ_{exL1} or ϕ_{exL2}. Two competing effects coexist in the GNSS-RO observations, and both are evident in the E-region ϕ_{exL1} and ϕ_{exL2} measurements shown in [Wu, 2018]. In these RO ϕ_{exL1} and ϕ_{exL2} profiles, the F-region effect manifests itself primarily as a phase delay that varies gradually with h_t while the phase advance from narrow sporadic-E layers is superimposed on the F-region variation.

Because path length changes and phase advances are coupled in GNSS-RO, especially for the radio wave propagation with a long path through a structured ionosphere, quantifying their relative importance in RIE is not trivial. Fig.A1 highlights the differences between bending-induced delay and plasma phase advance using an idealized geometry with and without bending. The bending can be upward and downward in the *F*-region, as the radio wave propagates across an interface with a large refractivity gradient [Fig.A1(a)]. The bending induces a pathlength change in the L1 and L2 propagation, and a subsequent phase delay. However, this delay is offset in the meantime by the phase advance from the radio propagation in plasma. The net effect would depend on how significant the bending is. In the case with little or insignificant bending, as in Fig.A1(b), a phase advance still exists and could be misinterpreted as an upward bending even though there is no bending. For a typical Chapman-layer ionosphere, Hoque and Jakowski [2011] found that the bending-induced ϕ_{exL1} error is about 1-2 m for the L1 frequency, while the phase advance over a long path length can be as high as 10's m or over 100 TECu (1 TECu = 0.162 m for L1).
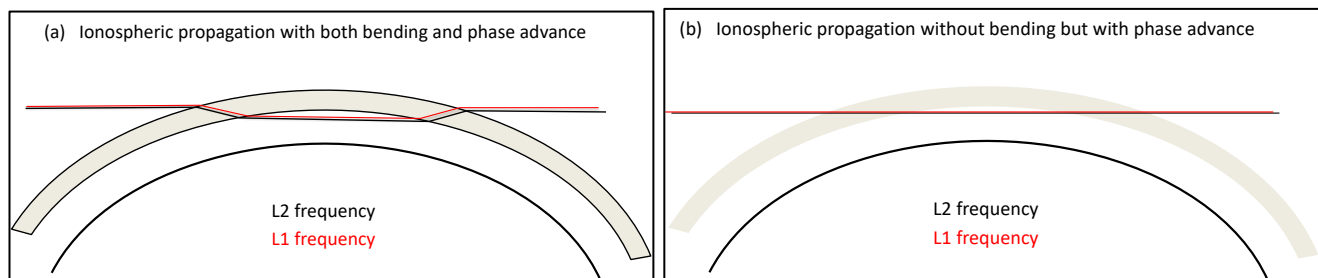
Fig.A1. Illustration of radio wave propagation through an idealized ionosphere (a) with and (b) without bending. A sharp vertical gradient in ionospheric electron density can induce a significant bending, whereas the bending is small and negligible

if the gradient is weak. Case (a) illustrates the bending from a sharp refractivity gradient between the vacuum and an ionospheric layer. Case (b) assumes a smooth/gradual transition between the vacuum and the ionosphere such that bending is negligible. In both cases the phase advance is significant and non-negligible (see text for more description).

670   **B. RIE Impacts on Mesospheric Temperature and Winds**

Solar migrating tides dominate the diurnal variation in the upper atmospheric temperature and winds. Thus, it is imperative to assess the relative importance of RIE impact as a function of local time. Figs.B1-B2 show the local time variations of temperature at 1 and 0.1 hPa where the GNSS-RO RIE errors can be very large, compared to the mean α. Interestingly, the local time variations from experiments NoGPS and BiasLST look very similar to that from the Control experiment, despite

675 large differences in the zonal mean temperatures. The experiment with a very large (BiasM2) appears to damp the diurnal amplitude by 30-50%. Otherwise, the experiments with NoGPS and BiasLST do not seem to significantly change the tidal phase in LST because the dominant migrating tidal modes are locked in phase to the solar forcings in the troposphere and stratosphere.

Despite a relaxed value used in the DA covariance matrix in assimilating GNSS-RO α from higher altitudes, the

680 measurement errors such as RIE still have a significant impact on the assimilated winds and temperatures at pressures < 5 hPa. For example, in Fig.B3 the CTL – NoGPS difference suggests that the GNSS-RO data made an equatorward shift of the polar vortex near 0.2 hPa in the northern hemisphere winter. In the presence of a RIE like BiasLST, this shift becomes larger at pressures > 0.2 hPa but in the poleward direction at <0.2 hPa. In the southern hemisphere, the BiasLST makes the zonal winds shifted significantly equatorward. Because the reanalysis data have been widely used at these pressure levels (1 – 0.1 hPa), it

685 would require a special attention to the RIE impact during the period when GNSS-RO data are assimilated.
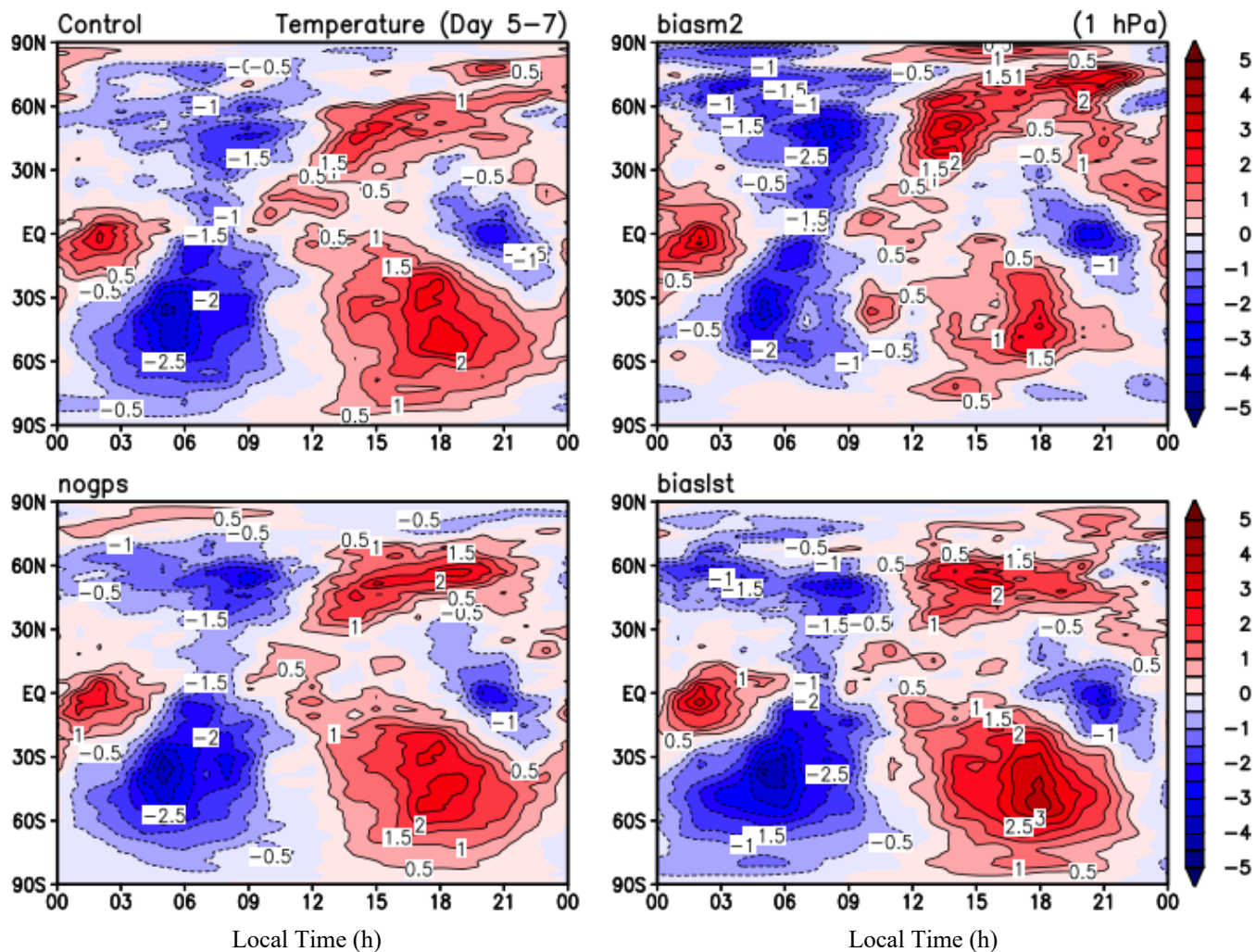
Fig.B1. Diurnal temperature variations from the controlled and perturbed experiments at 1 hPa. The temperature perturbations from its zonal mean in K are contoured in color.
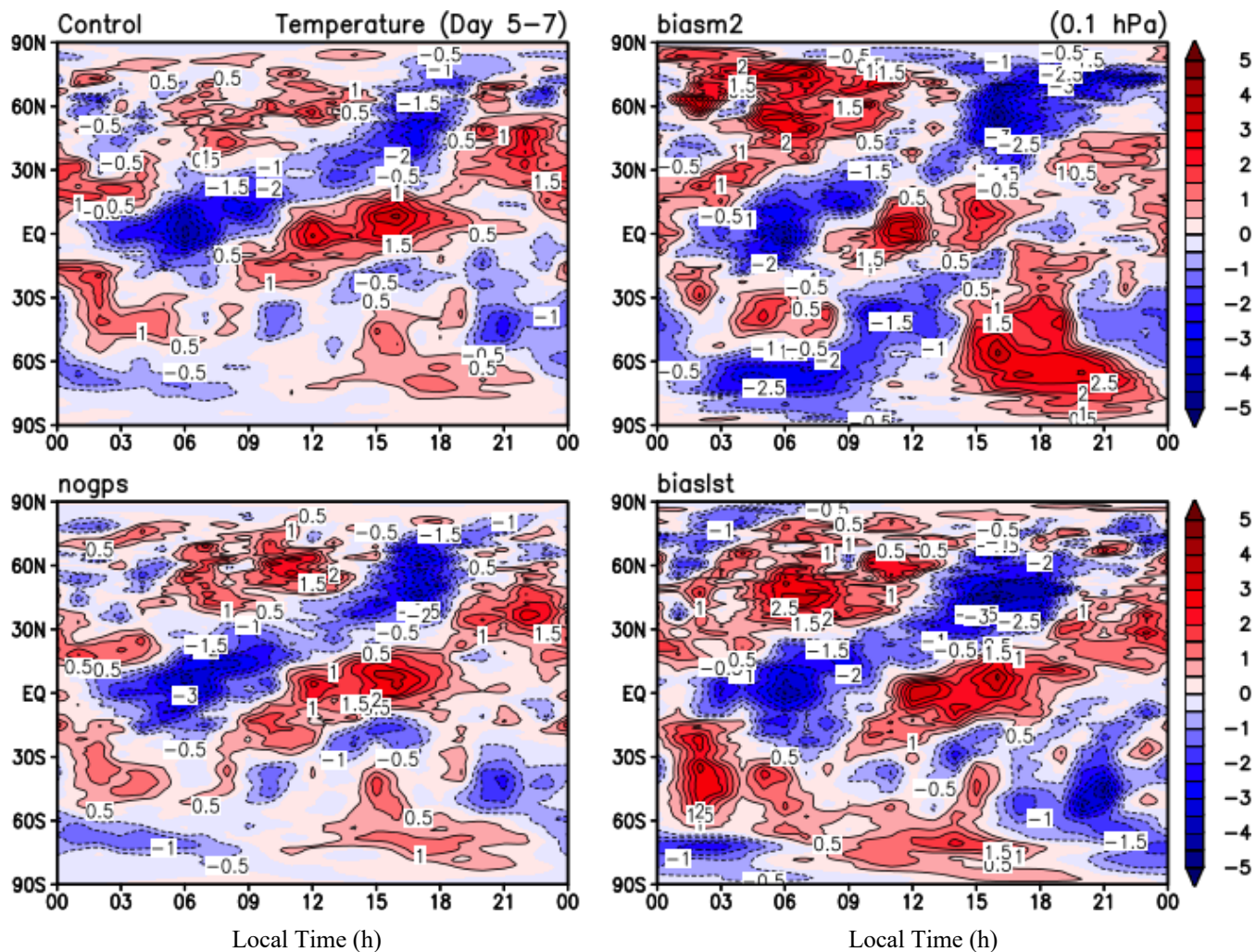
Fig.B2. As in Fig.B1 but for 0.1 hPa.
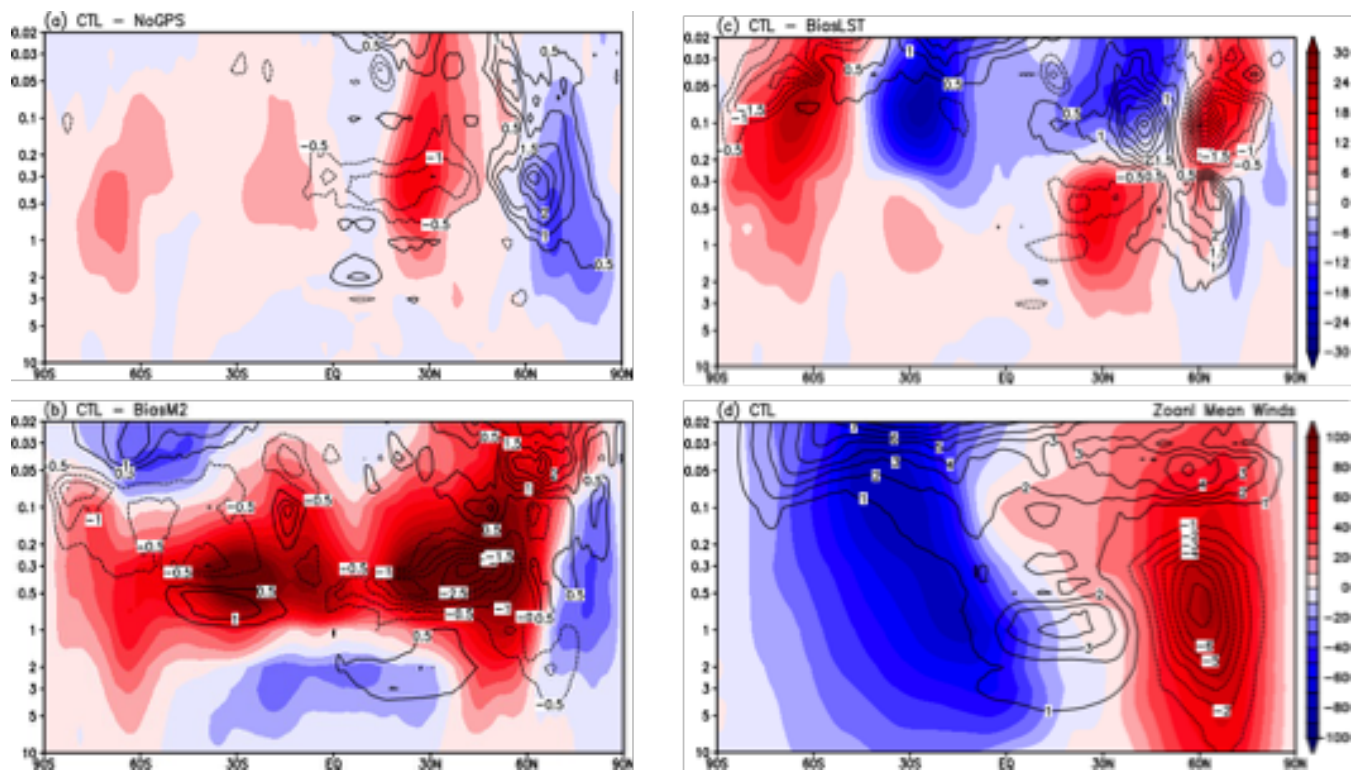
695

Fig.B3. Impacts of the RIEs on upper-atmospheric winds at 10-0.02 hPa from the DA experiments: (a) CTL-NoGPS, (b) CTL – BiasM2, and (c) CTL – BiasLST, sharing the same color scale in panel (c). The mean wind from CTL is displayed in (d). All panels have the zonal winds contoured in color with unit of m/s, superimposed by the meridional winds contoured by lines.

C. GNSS-RO Mission Summary

700   The global GNSS-RO observations can be perhaps divided into three periods in terms of the total number of daily RO profiles: CHAMP-period (2001-2006), COSMIC1-period (2006-2019), COSMIC2-commercial-period (2019-). Advances in commercial RO receiver technologies play a critical role in the increase of the number of RO acquisitions from space in recent years. The BlackJack RO receiver on CHAMP, developed by NASA Jet Propulsion Laboratory (JPL), was able to track a dual-frequency GPS (G) signals for precise (cm accuracy range) orbit determination and continuous coverage [Hajj et al., 2004].

705 For the RO observation, the receiver software was also able to schedule high-rate (50 Hz) tracking of setting occultations of up to four GPS satellites. The BlackJack on CHAMP has only aft antennas for the RO sounding, which yielded ~250 profiles per day. The sampling was further improved by tracking rising occultations with the open-loop (OL) tracking successfully demonstrated on the SAC-C and later COMSIC-1 satellites. This advance led to the dual-antenna (aft and fore) and OL tracking IGOR (Integrated GPS and Occultation Receiver) implemented by the COMSIC-1 constellation [BRE, 2003], which produced

710 ~700 daily ROs per satellite, or an average total of ~4000 daily ROs from ta six-satellite constellation.

The recent boost in the number of GNSS-RO observations came from availability of civil signals provided by GNSS satellites [GLONASS (R), Galileo (G), and BDS (C)], and from the combination of a new four-antenna TriG (Tri-band GNSS) receiver [Esterhuizen et al., 2009] on COSMIC-2 and commercial CubeSat constellations. While operational weather satellites such as MetOp [Zus et al., 2011] and FY3 [Bai et al., 2014] continue to provide global GNSS-RO observations, the commercial
715 data from SmallSat/CubeSat constellations provided by Spire [Angling et al., 2021], GeoOptics [Chang et al., 2022], and PlanetiQ [Kursinski et al., 2021] have become increasingly important to yield the needed spatiotemporal coverage on the globe. The maximum RO top height, listed in Table A1 for these missions, is a key parameter to derive the RIE with the $d\phi_{ex}/dh_t$ method presented in this study.

Table A1. Summary of GNSS-RO data used in this study

LEO Satellites	Mission lifetime	Init,Final Alt (km)	Sun-syn (Asc ECT[1])	Lat Coverage	Top RO Ht (km)	Tracked GNSS	Daily No. ROs
CHAMP	2001-2008	450,330	varying	90°S/N	140	G	~250
COSMIC-1[2]	2006-2020	525,810	varying	90°S/N	130	G	~4000
SAC-C	2000-2013	705	10:30	90°S/N	90	G	100-300
MetOp-A[3]	2006-2021	820	19:00	90°S/N	90,300	G	~720
MetOp-B[3]	2012-	820	19:00	90°S/N	90,300	G	~700
MetOp-C[3]	2018-	820	19:00	90°S/N	90,300	G	~650
C/NOPS	2008-2015	850,350	varying	37°S/N	170	G	~300
KOMPSAT-5	2015-	560	06:00	90°S/N	135	G	300-600
TSX	2009-	520	18:00	90°S/N	135	G	150-300
TDX	2016-	520	18:00	90°S/N	135	G	150-300
GRACE	2007-2017	475,300	varying	90°S/N	140	G	100-250
FY-3C[4]	2013-	838,850	22:00	90°S/N	130	G	400-550
FY-3D	2017-	838	13:30	90°S/N	130	G	400-600
FY-3E[5]	2021-	830	05:30	90°S/N	130	G, C	~1100
FY-3F[5]	2023-	830	13:30	90°S/N	130	G, C, E	~1600
FY-3G	2023-	414	varying	40°S/N	130	G, C, E	1200-1600
COSMIC-2[6]	2019-	715,540	varying	44°S/N	90-500	G,R	~6500
PAZ	2018-	520	18:00	90°S/N	135	G	200-300
Sentinel-6A	2020-	1336	varying	90°S/N	80	G,R	~800
GeoOptics	2020-2022	490	varying	90°S/N	145	G	300-1800

| Spire[7] | 2018- | 500-600 | varying | 90°S/N | 170-600 | G,R,E,J,C | ~4000[8] ~12,000[8] |
| PlanetiQ | 2023- | ~500 | varying | 90°S/N | 170 | G,R,E,C | 1000-3800 |

[1] Ascending-orbit equator crossing time (Asc ECT)

[2] The COSMIC1-3 spacecraft never reached the intended orbital altitude and was operated at 725km for the rest of its mission.

[3] Metop-A started to drift away from the Sun-sync orbit since ~2021. An extended RO experiment with Metop-A to acquire the high-rate data up to h_t=300km during 2020D161-2020D254. Following the successful experiment, the high-top RO acquisition has been implemented for the routine operation in MetOp-B/C since 2021.

[4] FY-3C started to drift away from the Sun-sync orbit (SSO) since 2016.

[5] FY-3E started to track GPS (G) and BDS (C), and FY-3F and 3G started to track GPS (G), BDS (C), and Galileo (E)

[6] The CDAAC COSMIC-2 NRT data contain GNSS-RO profiles from GPS (G) and GLONASS (R). The nominal RO top is ~140 km, but occasionally reaches up to 300 km or 500 km for space weather measurements.

[7] The Spire GNSS-RO observation tracks GPS (G), GLONASS (R), Galileo (E), and BDS (C) signals routinely to ~170 km, but for space weather observations the tracking often goes up to 300, 350, 500 or 600 km. The tracking of and QZSS (J) occurred briefly before 2021.

[8] NASA's Commercial Smallsat Data Acquisition (CSDA) data have a larger number of post-processing RO profiles per day from November 2019 to the present. The NOAA Commercial Data Program (CDP) acquires a fewer number of near-real-time (NRT) RO profiles per day, compared to the CSDA archive.
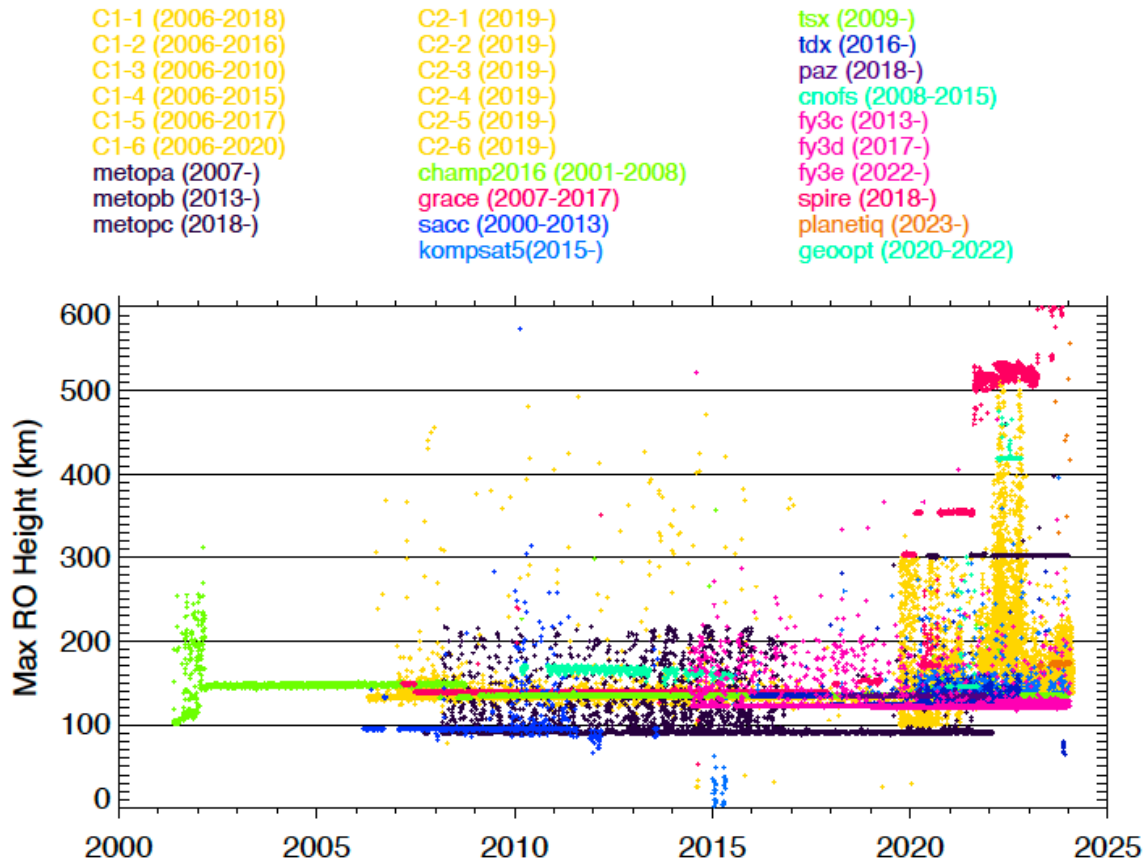
Fig.A1. Daily GNSS-RO statistics of the maximum RO top height from the past and current missions in 2001-2023.

Competing interests

The contact author has declared that none of the authors has any competing interests.

Acknowledgements

The work was by supported partially by NASA Goddard Space Flight Center (GSFC) Science Task Group (STG) fund and Commercial Smallsat Data Acquisition (CSDA) program. The authors thank UCAR COSMIC Data Analysis and Archive Center (CDAAC), EUMETSAT Radio Occultation Meteorology Satellite Application Facility (ROM SAF) and China Meteorological Administration (CMA) National Satellite Meteorological Center (NSMC) services for GNSS-RO data processing and distribution.

References

Angling, M. J., Elvidge, S., & Healy, S. B. (2018). Improved model for correcting the ionospheric impact on bending angle in radio occultation measurements. Atmospheric Measurement Techniques, 11, 2213–2224. https://doi.org/10.5194/amt-11-2213-2018

Angling, M. J., et. al. (2021). Sensing the ionosphere with the Spire radio occultation constellation, J. Space Weather Space Clim. 11 56, DOI: 10.1051/swsc/2021040

Arras, C., C. Jacobi, J. Wickert (2009), Semidiurnal tidal signature in sporadic E occurrence rates derived from GPS radio occultation measurements at higher midlatitudes. Ann. Geophys. 27, 2555–2563.

Bai, W. H., et al., An introduction to the FY3 GNOS instrument and mountain-top tests, Atmos. Meas. Tech., 7, 1817–1823, https://doi.org/10.5194/amt-7-1817-2014, 2014

Bonavita, M., 2014: On some aspects of the impact of GPSRO observations in global numerical weather prediction. Quart. J. Roy. Meteor. Soc., 140, 2546–2562, doi:10.1002/qj.2320.

BRE, Integrated GPS occultation receiver IGOR; data sheet. Broadreach Engineering, Tempe, Arizona, 2003.

Brunner, F. K. & Gu, M. (1991). An improved model for the dual frequency ionospheric correction of GPS observations. manuscripta geodaetica, Vol. 16, No. 3, pp. (205- 214)

Chang, H., Lee, J., Yoon, H. et al. Performance assessment of radio occultation data from GeoOptics by comparing with COSMIC data. Earth Planets Space 74, 108 (2022). https://doi.org/10.1186/s40623-022-01667-6

Coleman, C. J., and B. Forte (2017), On the residual ionospheric error in radio occultation measurements, Radio Sci., 52, 918–937, doi:10.1002/ 2016RS006239

Cucurull, L., J. C. Derber, and R. J. Purser, 2013: A bending angle forward operator for global positioning system radio occultation measurements. J. Geophys. Res. Atmos., 118, 14–28, doi:10.1029/2012JD017782.

Cucurull, L., and R. A. Anthes, 2015: Impact of Loss of U.S. Microwave and Radio Occultation Observations in Operational Numerical Weather Prediction in Support of the U.S. Data Gap Mitigation Activities. Wea. Forecasting, 30, 255–269, https://doi.org/10.1175/WAF-D-14-00077.1

Cucurull, L., R. A. Anthes, and L. Tsao, 2014: Radio Occultation Observations as Anchor Observations in Numerical Weather Prediction Models and Associated Reduction of Bias Corrections in Microwave and Infrared Satellite Observations. *J. Atmos. Oceanic Technol.*, 31, 20–32, https://doi.org/10.1175/JTECH-D-13-00059.1

Culverwell, I., H. Lewis, D. Offiler, C. Marquardt, and C. Burrows, 2015: The radio occultation processing package, ROPP. Atmos. Meas. Tech., 8, 1887–1899, https://doi.org/10.5194/amt-8-1887-2015.

Danzer, J., Scherllin-Pirscher, B., & Foelsche, U. (2013). Systematic residual ionospheric errors in radio occultation data and a potential way to minimize them. Atmospheric Measurement Techniques, 6(8), 2169–2179. https://doi.org/10.5194/amt-6-2169-2013

Danzer, J., Schwaerz, M., Kirchengast, G., & Healy, S. B. (2020). Sensitivity analysis and impact of the kappa-correction of residual ionospheric biases on radio occultation climatologies. Earth and Space Science. 7, e2019EA000942. https://doi.org/ 10.1029/2019EA000942

Danzer, J., Haas, S. J., Schwaerz, M., & Kirchengast, G. (2021). Performance of the ionospheric kappa-correction of radio occultation profiles under diverse ionization and solar activity conditions. Earth and Space Science, 8, e2020EA001581. https://doi.org/10.1029/2020EA001581

Dee, D. P., Uppala, S. M., Simmons, A. J., Berrisford, P., Poli, P., Kobayashi, S., et al. (2011). The ERA-Interim reanalysis: Configuration and performance of the data assimilation system. Quarterly Journal ofthe royal meteorological society, 137(656), 553–597. https://doi.org/ 10.1002/qj.828

Esterhuizen, S., Franklin, G., Hurst, K., Mannucci, A., Meehan, T., Webb, F., Young, L., "TriG - A GNSS Precise Orbit and Ra-dio Occultation Space Receiver," Proceedings of the 22nd International Technical Meeting of The Satellite Division of the In-stitute of Navigation (ION GNSS 2009), Savannah, GA, September 2009, pp. 1442-1446.

790 Foelsche, U., Scherllin-Pirscher, B., Ladstädter, F., Steiner, A. K., & Kirchengast, G. (2011). Refractivity and temperature climate records from multiple radio occultation satellites consistent within 0.05%. Atmospheric Measurement Techniques, 4, 2007–2018. https://doi.org/10.5194/amt-4-2007-2011

Forbes, J. M., J. Russell, S. Miyahara, X. Zhang, S. Palo, M. Mlynczak, C. J. Mertens, and M. E. Hagan (2006), Troposphere-thermosphere tidal coupling as measured by the SABER instrument on TIMED during July–September 2002, J. Geophys. Res., 111, A10S06,
795 doi:10.1029/2005JA011492.

Gelaro, R., et al. (2017) The modern-era retrospective analysis for research and applications, version 2 (MERRA-2). Journal of Climate, 30(14), 5419–5454.

Gleisner, H., Ringer, M.A. & Healy, S.B. Monitoring global climate change using GNSS radio occultation. npj Clim Atmos Sci 5, 6 (2022). https://doi.org/10.1038/s41612-022-00229-7

800 Gong, J., D. L. Wu, and S. D. Eckermann (2012), Gravity wave variances and propagation derived from AIRS radiances, Atmos. Chem. Phys., 12(4), 1701–1720.

Gorbunov, M. E., Ionospheric correction and statistical optimization of radio occultation data, Radio Sci., 37(5), 1084, doi:10.1029/2000RS002370, 2002

Hajj, G. A., and L. J. Romans (1998), Ionospheric electron density profiles obtained with the Global Positioning System: Results from the
805 GPS/MET experiment, Radio Sci., 33, 175–190, doi:10.1029/97RS03183.

Hajj, G. A., C. O. Ao, B. A. Iijima, D. Kuang, E. R. Kursinski, A. J. Mannucci, T. K. Meehan, L. J. Romans, M. de la Torre Juarez, and T. P. Yunck (2004), CHAMP and SAC-C atmospheric occultation results and intercomparisons, J. Geophys. Res., 109, D06109, doi:10.1029/2003JD003909.

Hartmann, G. K. & Leitinger, R. (1984). Range errors due to ionospheric and tropospheric effects for signal frequencies above 100 MHz.
810 Bull. Geod, Vol 58, No. 2, pp. (109- 136)

Hersbach, H., Bell, B., Berrisford, P., Hirahara, S., Horányi, A., Muñoz-Sabater, J., et al. (2020). The ERA5 global reanalysis. Quarterly Journal of the Royal Meteorologic Healy, S. B.,

Healy, S. B., A. M. Jupp, and C. Marquardt (2005), Forecast impact experiment with GPS radio occultation measurements, Geophys. Res. Lett., 32, L03804, doi:10.1029/2004GL020806.

815 Healy, S. B., J. R. Eyre, M. Hamrud, and J-N. Thepaut, 2007: Assimilating GPS radio occultation measurements with two-dimensional bending angle observation operators. Quart. J. Roy. Meteor. Soc., 133 , 1213–1227.

Healy, S. B. and Culverwell, I. D.: A modification to the standard ionospheric correction method used in GPS radio occultation, Atmos. Meas. Tech., 8, 3385–3393, https://doi.org/10.5194/amt- 8-3385-2015, 2015.

Hoque, M.M., Jakowski, N. Higher-order ionospheric effects in precise GNSS positioning. J. Geodesy 81 (4), 259–268, doi:10.1007/s00190-
820 006-0106-0, 2007.

Hoque, M. M., and N. Jakowski (2011), Ionospheric bending correction for GNSS radio occultation signals, Radio Sci., 46, RS0D06, doi:10.1029/2010RS004583.

Immel, T. J., E. Sagawa, S. L. England, S. B. Henderson, M. E. Hagan, S. B. Mende, H. U. Frey, C. M. Swenson, and L. J. Paxton (2006), Control of equatorial ionospheric morphology by atmospheric tides, Geophys. Res. Lett., 33, L15108, doi:10.1029/2006GL026161.

825 Kindervatter, T.H. and Teixeira, F.L. (2022). Overview of the Global Positioning System. In Tropospheric and Ionospheric Effects on Global Navigation Satellite Systems (eds T.H. Kindervatter and F.L. Teixeira). https://doi.org/10.1002/9781119863069

Kursinski, E. R., Hajj, G. A., Schofield, J. T., Linfield, R. P., & Hardy, K. R. (1997). Observing Earth's atmosphere with radio occultation measurements using the Global Positioning System. Journal of Geophysical Research, 102, 23429–23465. https://doi.org/10.1029/97JD01569

830 Kursinski, E. R., et al. (2021). Initial Results and Validation of PlanetiQ GNSS RO Neutral Atmosphere Measurements. AGU Fall Meeting 2021, held in New Orleans, LA, 13-17 December 2021, id. A25L-1839.

Ladreiter, H.-P., Kirchengast, G. GPS/GLONASS sensing of the neutral atmosphere: model independent correction of ionospheric influences. Radio Sci. 31 (4), 877–891, 1996.

Leroy, S. S., & Gleisner, H. (2022). The stratospheric diurnal cycle in COSMIC GPS radio occultation data: Scientific applications. Earth
835 and Space Science, 9, e2021EA002011. https://doi.org/10.1029/2021EA002011

Li, M., Yue, X., Wan, W., & Schreiner, W. S. (2020). Characterizing ionospheric effect on GNSS radio occultation atmospheric bending angle. Journal of Geophysical Research, 125(6), e2019JA027471. https://doi.org/10.1029/2019JA027471

Liu, C., Kirchengast, G., Syndergaard, S., Schwaerz, M., Danzer, J., & Sun, Y. (2020). New higher-order correction of GNSS RO bending angles accounting for ionospheric asymmetry: Evaluation of performance and added value. Remote Sensing, 12, 3637.
840 https://doi.org/10.3390/rs12213637

Mannucci, A. J., Ao, C. O., Pi, X., and Iijima, B. A.: The impact of large scale ionospheric structure on radio occultation retrievals, Atmos. Meas. Tech., 4, 2837–2850, https://doi.org/10.5194/amt- 4-2837-2011, 2011.

Melbourne, W. G., E. Davis, C. Duncan, G. Hajj, K. Hardy, E. Kursinski, T. Meehan, L. Young, T. P. Yunck, The application of space borne GPS to atmospheric limb sounding and global change monitoring, JPL Publ., 94- 18, 147 pp., 1994.

845 Melbourne, W. G., Radio Occultations Using Earth Satellites: A Wave Theory Treatment. Jet Propulsion Laboratory California Institute of Technology, Monograph 6, Deep space communications and navigation series, edited by: Yuen, J. H., 610 pp., 2004.

Morton, Y. T., Q. Zhou, and F. van Graas (2009), Assessment of second- order ionosphere error in GPS range observables using Arecibo incoher- ent scatter radar measurements, Radio Sci., 44, RS1002, doi:10.1029/ 2008RS003888.

Poli, P. P., S. B. Healy, and D. P. Dee, 2010: Assimilation of global positioning system radio occultation data in the ECMWF ERA-Interim
850 reanalysis. Quart. J. Roy. Meteor. Soc., 136, 1972–1990, doi:10.102/qj.172.

Purser, R. J., D. Parrish and M. Masutani, 2000: Meteorological observational data compression; an alternative to conventional "super-obbing". Office Note 430, National Centers for Environmental Prediction, Camp spring, MD [available online at http://wwwt.emc.ncep.noaa.gov/officenotes/FullT OC.html#2000]

Qu, X., Li, Z., An, J., & Ding, W. (2015). Characteristics of second-order residual ionospheric error in GNSS radio occultation and its impact
855 on inversion of neutral atmospheric parameters. Journal of Atmospheric and Solar-Terrestrial Physics, 130–131, 159–171. https://doi.org/10.1016/j.jastp.2015.05.016

Ringer, M. A. and Healy, S. B.: Monitoring twenty-first century cli- mate using GPS radio occultation bending angles, Geophys. Res. Lett., 35, 5, 2008.

Schmidt, T., de la Torre, A., and Wickert, J.: Global gravity wave activity in the tropopause region from CHAMP radio occultation data,
860 Geophys. Res. Lett., 35, L16807, https://doi.org/10.1029/2008GL034986, 2008.

Sokolovskiy, S., Schreiner, W., Rocken, C., and Hunt, D.: Optimal noise filtering for the ionospheric correction of GPS radio occultation signals, J. Atmos. Ocean. Tech., 26, 1398–1403, doi:10.1175/2009JTECHA1192.1, 2009.

Syndergaard, S. (2000). On the ionosphere calibration in GPS radio occultation measurements. Radio Science, 35(3), 865–883. https://doi.org/10.1029/1999rs002199

865 Syndergaard, S., & Kirchengast, G. (2022). Systematic ionospheric residual errors in GNSS radio occultation: Theory for spherically stratified media. Earth and Space Science, 9, e2022EA002335. https://doi.org/10.1029/2022EA002335

Tsuda, T., et al. (2000), A global morphology of gravity wave activity in the stratosphere revealed by the GPS Occultation data (GPS/MET), J. Geophys. Res., 105, 7257–7273.

Vergados, P., and S. D. Pagiatakis (2011), Latitudinal, solar, and vertical variability of higher-order ionospheric effects on atmospheric parameter retrievals from radio occultation measurements, J. Geophys. Res., 116, A09312, doi:10.1029/2011JA016573.

Vorob'ev, V. V. and Krasil'nikova, G. K.: Estimation of the accu- racy of the atmospheric refractive index recovery from doppler shift measurements at frequencies used in the NAVSTAR system, USSR Phys. Atmos. Ocean, Engl. Transl., 29, 602–609, 1994.

Wu, D. L., C. O. Ao, G. A. Hajj, M. de la Torre Juarez, and A. J. Mannucci (2005), Sporadic E morphology from GPS-CHAMP radio occultation, J. Geophys. Res., 110, A01306, doi: 10.1029/2004JA010701.

Wu, D. L., Small-scale fluctuations and scintillations in high-resolution GPS SNR and phase data, J ATMOS SOL-TERR PHY 68 (9), 999-1017, doi:10.1016/j.jastp.2006.01.006, 2006.

Wu, D. L. (2018), New global electron density observations from GPS-RO in the D- and E-Region ionosphere. *JASTP*, 1-24. DOI: http://dx.doi.org/10.1016/j.jastp.2017.07.013

Wu, D. L. and Eckermann, S. D.: Global gravity wave variances from Aura MLS: characteristics and interpretation, J. Atmos. Sci., 65, 3695–3718, 2008.

Zeng, Z., Sokolovskiy, S., Schreiner, W., Hunt, D., Lin, J., and Kuo, Y.-H.: Ionospheric correction of GPS radio occultation data in the troposphere, Atmos. Meas. Tech., 9, 335–346, https://doi.org/10.5194/amt-9-335-2016, 2016

Zou, L., H. Rishbeth, I. C. F. Muller-Wodarg, A. D.Aylward, G. H. Millward, T. J. Fuller-Rowell, D. W. Idenden, and R. J. Moffett (2000), Annual and semiannual variations in the ionospheric F2-layer: I. Modelling, Ann. Geophys., 18, 927–944, doi:10.1007/s00585-000-0927-8.

Zus F., Beyerle G., Heise S., Schmidt T., Wickert J., Marquardt C.: Validation of refractivity profiles derived from GRAS raw-sampling data, Atmos. Meas. Tech., 4, 1541-1550, 2011